CHALMERS
UNIVERSITY OF TECHNOLOGY

Model Predictive Control of Electric Machines in Commercial Vehicles

Electric Power Engineering

DUO XU
YAO CAI

Department of Electrical Engineering
CHALMERS UNIVERSITY OF TECHNOLOGY
Gothenburg, Sweden 2019

Master's thesis 2019:NN

Model Predictive Control of Electric Machines in Commercial Vehicles

DUO XU
YAO CAI

Department of Electrical Engineering
Electric Power Engineering
Chalmers University of Technology
Gothenburg, Sweden 2019

Model Predictive Control of Electric Machines in Commercial Vehicles

DUO XU
YAO CAI

Supervisor:
Jonas Ottosson, Motor Drive Systems, Volvo Group Trucks Technology
Faisal Altaf, Control Systems, Volvo Group Trucks Technology

Examiner:
Torbjorn Thiringer, Department of Electrical Engineering,
Chalmers University of Technology

Master's Thesis 2019
Department of Electrical Engineering
Electric Power Engineering
Chalmers University of Technology
SE-412 96 Gothenburg
Telephone +46 31 772 1000

Typeset in LaTeX
Gothenburg, Sweden 2019

Model Predictive Control of Electric Machines in Commercial Vehicles
DUO XU
YAO CAI
Department of Electrical Engineering
Chalmers University of Technology

Abstract

This thesis focuses on the realization of a Finite Control Set Model Predictive Control (FCS-MPC) scheme for a benchmark electric drive system which is supported by Volvo Group. A Permanent Magnet Synchronous Machine (PMSM) is used in this electric drive system, the non-linear model of the PMSM is derived after taking the magnetic saturation and the cross-coupling effects into consideration. Certain characteristic trajectory functions of the PMSM control strategies such as Maximum Torque Per Ampere (MTPA), Field Weakening (FW) and Maximum Torque Per Volt (MTPV) are formulated based on the non-linear PMSM model. A two-level Voltage Source Inverters (VSI) without modulation scheme has 8 switching states in total to generate the input voltage for the PMSM. In order to reduce the switching losses, assumption has been made that at most one of the three inverter phase legs is allowed to change its switching state between each two sampling instances. The future system states can be predicted with the finite set of the possible input voltages and the discretized PMSM model. A multi-objective cost function is introduced to derive the optimal voltage input at the next time step. The cost function deals with three targets: torque tracking, attraction region and limitation. The torque tracking part enables the PMSM to generate the reference torque. The attraction region part forces the current states to evolve on the desired operation trajectory which is depend on the torque and speed level. The limitation part aims to avoid the current states reaching undesired operation regions. A PI controller has been designed for the benchmark electric drive system, the operation performances are compared between the FCS-MPC and PI based on the aspects of step response, tracking correctness, switching losses, current ripple and torque ripple. Though the ripple performance of the FCS-MPC is not as well as that of the PI, FCS-MPC helps to realize a faster rise time and lower switching losses. Evaluations of the FCS-MPC are also included with respect to different sampling frequencies and prediction horizons, which mainly affect the performance of tracking correctness along different trajectories.

Keywords: Finite control set model predictive control, permanent magnet synchronous machine, flux saturation, cross-coupling effect, maximum torque per ampere, field weakening, maximum torque per volt, two-level voltage source inverters, switching losses

Acknowledgements

This thesis was conducted at Volvo Group in Gothenburg, Sweden and the department of Electrical Engineering at Chalmers University of Technology. First we want to give great gratitude to our supervisor Dr. Jonas Ottosson and Dr. Faisal Altaf. Their patient instruction and continuous support accompanied us all the way through this master thesis. And we are also very grateful to our examiner at Chalmers University of Technology, Prof. Torbjörn Thiringer, who is always trying to help us with different kinds of questions and give good suggestions to the thesis. Finally, we have to express appreciation to our friends and parents who always show us unconditional encouragement and love at every stage of our lives. Without all these people we would not be able to accomplish the thesis successfully.

Duo Xu and Yao Cai, Gothenburg, June 2019

Contents

1

Introduction

1.1 Motivation

Various vehicles have brought a lot of convenience to people's life, and with the invention of the internal combustion engine, pure fuel vehicle is widely popularized. However, these type of vehicles are associated with some environmental issues such as air pollution and green house gases. According to statistics, transportation contributes to almost a quarter of greenhouse gas emissions in Europe and is the main cause of air pollution in cities[1]. Meanwhile, the supply of non-renewable resources keep reducing and the price keeps going up. So in recent years, electric mobility plays a more important role in today's society, since electricity can be used at high efficiency and electricity that comes from renewable resource can reduce carbon dioxide significantly. These advantages make electric vehicles (EV) a good way to deal with the steady increase in fuel prices, strict carbon constraints, and increasing environmental concerns. Also, the technology development within electric mobility makes it possible to replace the pure fuel vehicles[2].

All the vehicles that can be recharged externally can be seen as electric mobility, which can be divided into three main types. The first type is the purely electric vehicles. The second type is the vehicles with a combination of electric motor and a small combustion engine (range extended electric vehicles-REEV). And the third type is the hybrid vehicles that can be recharge via the power grid (plug-in hybrid electric vehicles-PHEV)[3]. In all types of electric mobility, the electric drive system is a key system consisting of a least one electric machine and a dedicated power electronic inverter.

The main functionality for the electric drive system is to realize a torque or speed request with high efficiency high torque quality and low impact on other sub-systems. And the control of the electric drive system has a strong influence on drivability, efficiency, lifetime and noise. Classical electric machine control is based on Field Oriented Control (FOC) with standard PI-controllers as a base for controlling the current. However, this control scheme has difficulty handling strongly coupled electro-mechanical-thermal constraints of the electric drive system. And when multiple objectives need to be achieved within the FOC framework at the same time, such as voltage tracking, torque tracking with reduced ripple, minimization of switching losses, noise reduction and so on, the PI-controllers don't seem to work well. To deal with these problems, this thesis applies a relatively new type of control method called Finite Control Set Model Predictive Controller (FCS-MPC), whose core is based on mathematical optimization theory, and can solve multiple objectives as well as system constraints in a systematic way. Moreover, it takes into account the system dynamics and constraints in a prediction horizon.

1.2 Related work

So far, the MPC control scheme has been applied to various types of electric machines with different control methods and specified requirements[4]. In order to have a good performance of the MPC control scheme, an accurate model of the system is necessary. In fact, for a PMSM model in the dq coordinate system, the fluxes vary non-linearly with respect to the currents due to the saturation and cross coupling effects[5]. Various types of FCS-MPC control schemes can be implemented when a non-linear MPC model is used to predict the system states[6][7], the cost functions of the FCS-MPC can be formulated based on the current errors. This thesis is conducted based on formulating the cost functions of the current states errors when compared to certain featured current trajectories such as MTPA, Field Weakening and MTPV[8][9]. In this way, the reference currents are not needed to be derived at each sampling interval. Saturation and cross coupling effects are included in this thesis, and the featured current trajectories for the PMSM are reformulated based on non-linear flux.

1.3 Aim

In this thesis, the aim is to develop a framework called FCS-MPC that can realize good control of the electric drive system, meanwhile a FOC with PI-control of the currents will serve as a reference. In detail, the performance of the FCS-MPC is evaluated by step responses, current states trajectory tracking, current and torque quality, and inverter switching losses compared to those ones occurring when using the PI control scheme as a benchmark. Also, impact of sampling frequency and prediction horizon on the performance are analyzed.

1.4 Limitation

However, there are still some limitations of this FCS-MPC. The PMSM model used for the FCS-MPC is non-linear since it takes the magnetic saturation and cross-coupling effects into account. In addition, a larger prediction horizon leads to the exponential increase of the states prediction calculation. Both factors add computational effort and increase the execution time of the FCS-MPC. In order to reduce the switching frequency, only one of the three phase legs is permitted to change its switching state per sampling period in the two-level voltage source inverter (VSI). But this kind of VSI can lead to large ripples in the currents and torque because only one full length voltage vector is used during the switching period compared to the PI which changes the vector 6 times during a sampling period. One way to reduce torque ripple is to increase the sampling frequency, but then the less sampling time may not be enough to support the heavy computation of the FCS-MPC, which is not be desirable.

1.5 Outline

Chapter 2 introduces the theoretical knowledge of the PMSM and two-level VSI in the electric drive system. A non-linear PMSM model is derived which takes the magnetic saturation and the cross-coupling effects into account and its control strategies such as MTPA and FW are discussed to realize the PMSM operations at different conditions. Chapter 3 focuses on the execution of the FCS-MPC algorithm, a discretization model of the PMSM is utilized in the FCS-MPC to help predict the system states and find the optimal voltage input. Chapter 4 demonstrates the structure of the electric drive system and lists the main system parameters used for the simulation. In Chapter 5, a verification of the FCS-MPC model is made firstly to guarantee the proper simulation of the electric drive system. Simulation results are presented to compare the operation performances between the FCS-MPC and PI as well as the operation performances between different FCS-MPC configurations. In Chapter 6, conclusions of this thesis are drawn and a future work is proposed.

2

Theory

2.1 Introduction of the Permanent Magnetized Synchronous Machine

The Permanent Magnetized Synchronous Machine (PMSM) has been widely used in high-performance drive applications for their advantages such as high torque performance, high power density, free maintenance and so on. Compared with the Induction Machine (IM), the PMSM has a more complicated structure, and is difficult to be designed and analysed. Due to the flexible placement methods of the embedded magnets, there are different permanent magnet rotor configurations like Surface-mounted PMSM (SPM), Interior PMSM (IPM) and Permanent Magnet Assisted Synchronous Reluctance Machine (PMa-SynRM) as can be seen in Figure 2.1.

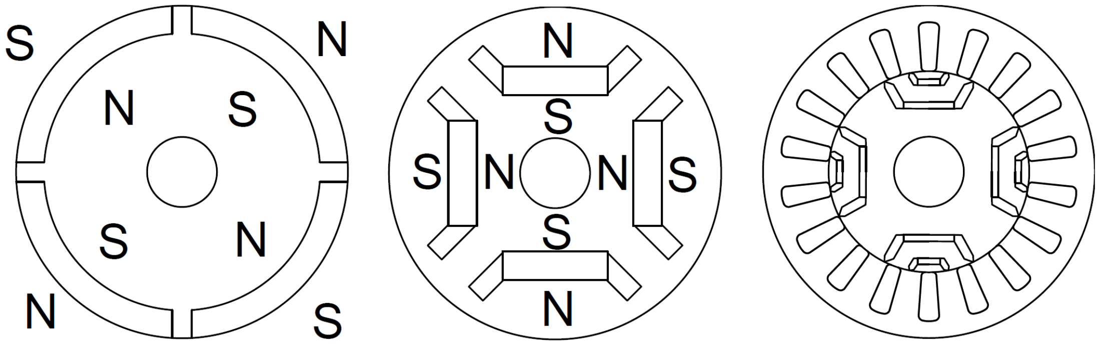

(a) SPM **(b)** IPM **(c)** PMa-SynRM

Figure 2.1: Three configurations of PMSM

This thesis deals with an IPM with its electrical parameters given and verified by the company Volvo Group.

2.1.1 Common coordinate systems for the analysis of PMSM

There are three commonly used coordinate systems for the modelling and analysis of the dynamic performance of electrical machines. Figure 2.2 shows the relations between the different coordinate systems.

1. abc three-phase stationary coordinate system
The three-phase windings are spatially located on the a-,b-,c- axes respectively. The stator electrical vector components such as voltage, current and flux hold their actual values on these axes. The rotor flux ψ_r rotates counter-clockwise in this coordinate system as the electrical speed ω_r is positive.

2. $\alpha\beta$ two-phase stationary coordinate system
The α-axis is aligned with the a-axis, the β-axis is 90° in advance of the α-axis. The rotor flux ψ_r rotates counter-clockwise in this coordinate system as the electrical speed ω_r is positive.

3. dq two-phase rotating coordinate
The orientation of the d-axis is aligned with the rotor flux ψ_r, the q-axis is 90° in advance. The dq coordinate system rotates counter-clockwise along the $\alpha\beta$ coordinate system with the same electrical speed ω_r of the rotor flux ψ_r, the electrical rotor angle θ_r is defined as the angle between the α-axis and the d-axis.

The dq two-phase rotating coordinate system helps in simplifying the analysis of the PMSM, since in this coordinate system, the electrical vector components are DC-quantities, standard control theories can be implemented under this precondition.

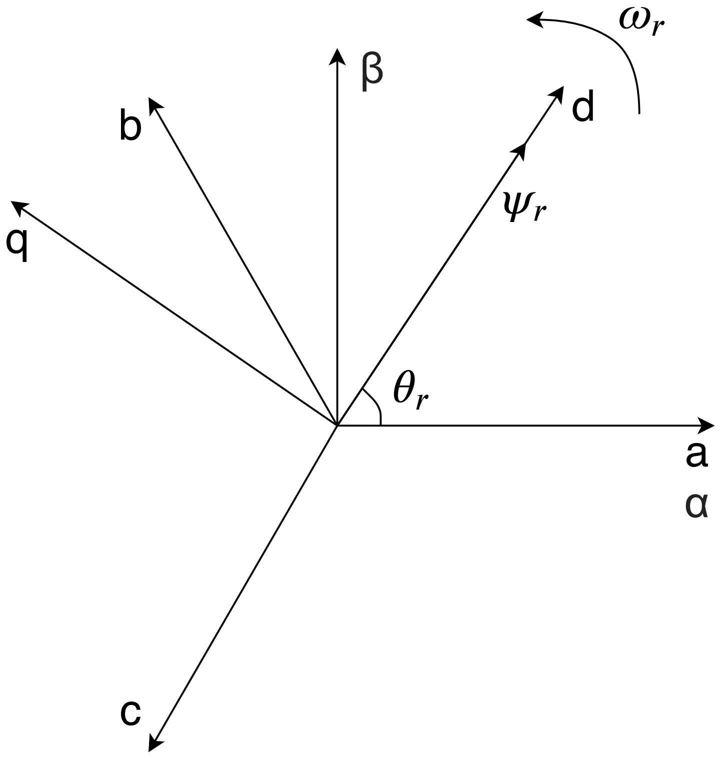

Figure 2.2: Relation between the three commonly used coordinate systems

There are two commonly used choices of coordinate system transformation, amplitude invariant transformation and power invariant transformation. The transformation functions are listed below.

1. Transformation between the abc and $\alpha\beta$ coordinate systems (Clarke transformation)
If three stator windings are completely symmetrical, the zero-vectors can be neglected, i.e., $x_a + x_b + x_c = 0$. Thus the transformation between the abc and $\alpha\beta$ coordinate systems can be simplified from the Clarke transformation as

$$\begin{bmatrix} x_\alpha \\ x_\beta \end{bmatrix} = C_{3s/2s} \begin{bmatrix} 1 & -\frac{1}{2} & -\frac{1}{2} \\ 0 & \frac{\sqrt{3}}{2} & -\frac{\sqrt{3}}{2} \end{bmatrix} \begin{bmatrix} x_a \\ x_b \\ x_c \end{bmatrix} \tag{2.1}$$

$$\begin{bmatrix} x_a \\ x_b \\ x_c \end{bmatrix} = C_{2s/3s} \begin{bmatrix} 1 & 0 \\ -\frac{1}{2} & \frac{\sqrt{3}}{2} \\ -\frac{1}{2} & -\frac{\sqrt{3}}{2} \end{bmatrix} \begin{bmatrix} x_a \\ x_\beta \end{bmatrix} \tag{2.2}$$

For the power invariant transformation, $C_{3s/2s} = \sqrt{\frac{2}{3}}$, $C_{2s/3s} = \sqrt{\frac{2}{3}}$. For the amplitude invariant transformation, $C_{3s/2s} = \frac{2}{3}$, $C_{2s/3s} = 1$.

2. Transformation between the $\alpha\beta$ and dq coordinate systems
Since the dq coordinate system rotates counter-clockwise along the $\alpha\beta$ coordinate system when the electrical speed ω_r is positive and the electrical rotor angle θ_r is defined as the angle between the α-axis and the d-axis, the transformation equations between these two coordinate systems are

$$\begin{bmatrix} x_d \\ x_q \end{bmatrix} = \begin{bmatrix} \cos\theta_r & \sin\theta_r \\ -\sin\theta_r & \cos\theta_r \end{bmatrix} \begin{bmatrix} x_a \\ x_\beta \end{bmatrix} \tag{2.3}$$

$$\begin{bmatrix} x_a \\ x_\beta \end{bmatrix} = \begin{bmatrix} \cos\theta_r & -\sin\theta_r \\ \sin\theta_r & \cos\theta_r \end{bmatrix} \begin{bmatrix} x_d \\ x_q \end{bmatrix} \tag{2.4}$$

3. Transformation between the abc and dq coordinate systems
Transformation between the abc and dq coordinate systems can be derived by combining (2.1), (2.2), (2.3) and (2.4), giving

$$\begin{bmatrix} x_d \\ x_q \end{bmatrix} = C_{3s/2s} \begin{bmatrix} \cos\theta_r & \cos(\theta_r - 120°) & \cos(\theta_r + 120°) \\ -\sin\theta_r & -\sin(\theta_r - 120°) & -\sin(\theta_r + 120°) \end{bmatrix} \begin{bmatrix} x_a \\ x_b \\ x_c \end{bmatrix} \tag{2.5}$$

$$\begin{bmatrix} x_a \\ x_b \\ x_c \end{bmatrix} = C_{2s/3s} \begin{bmatrix} \cos\theta_r & -\sin\theta_r \\ \cos(\theta_r - 120°) & -\sin(\theta_r - 120°) \\ \cos(\theta_r + 120°) & -\sin(\theta_r + 120°) \end{bmatrix} \begin{bmatrix} x_d \\ x_q \end{bmatrix} \tag{2.6}$$

For the power invariant transformation, $C_{3s/2s} = \sqrt{\frac{2}{3}}$, $C_{2s/3s} = \sqrt{\frac{2}{3}}$. For the amplitude invariant transformation, $C_{3s/2s} = \frac{2}{3}$, $C_{2s/3s} = 1$.

The amplitude invariant transformation is used throughout the whole thesis.

2.1.2 Modelling of the Permanent Magnetized Synchronous Machine

In this section, the modelling of the PMSM is carried out in the dq coordinate system, because the control scheme used in this thesis is analysed based on the dq coordinate system.

1. Electrical equations

The general voltage input equation of the PMSM in the dq coordinates can be expressed as

$$\begin{cases} u_d = R_s i_d + \frac{d\psi_d}{dt} - \omega_r \psi_q \\ u_q = R_s i_q + \frac{d\psi_q}{dt} + \omega_r \psi_d \end{cases} \tag{2.7}$$

For the standard way of modelling the PMSM with decoupled parameters, constant apparent inductances $(L_d(i_d), L_q(i_q) = \mathit{constant})$ and permanent magnetic flux linkage Ψ_m are introduced. This helps to formulate the flux linkages ψ_d, ψ_q as the following equations

$$\begin{gathered} \begin{cases} \psi_d = L_d i_d + \Psi_m \\ \psi_q = L_q i_q \end{cases} \\ \begin{cases} \frac{d\psi_d}{dt} = L_d \frac{di_d}{dt} \\ \frac{d\psi_q}{dt} = L_q \frac{di_q}{dt} \end{cases} \end{gathered} \tag{2.8}$$

By using (2.8) in (2.7), the standard model of the PMSM can be derived

$$\begin{cases} u_d = R_s i_d + L_d \frac{di_d}{dt} - \omega_r L_q i_q \\ u_q = R_s i_q + L_q \frac{di_q}{dt} + \omega_r L_d i_d + \omega_r \Psi_m \end{cases} \tag{2.9}$$

In contrast to the common assumption that the PMSM electrical parameters are decoupled, as Figure 2.3 reveals, taking magnetic saturation, cross-coupling and heat losses into account, the flux linkages ψ_d, ψ_q of the PMSM can vary non-linearly with respect to both dq coordinate currents i_d, i_q as well as the machine temperature T. The parameter variations of ψ_d, ψ_q have been recorded under certain tests, these values are stored in the form of LookUp-Tables (LUTs): $\psi_d(i_d, i_q, T)$, $\psi_q(i_d, i_q, T)$ and $R_s(T)$.

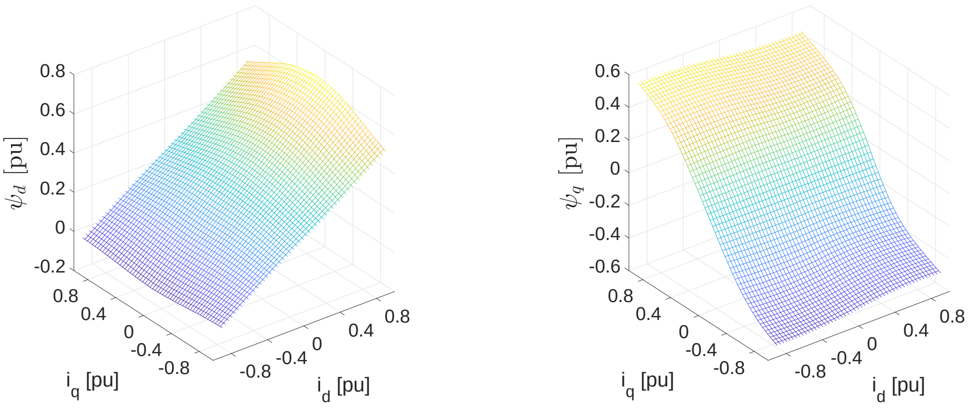

(a) Mesh plot of ψ_d **(b)** Mesh plot of ψ_q

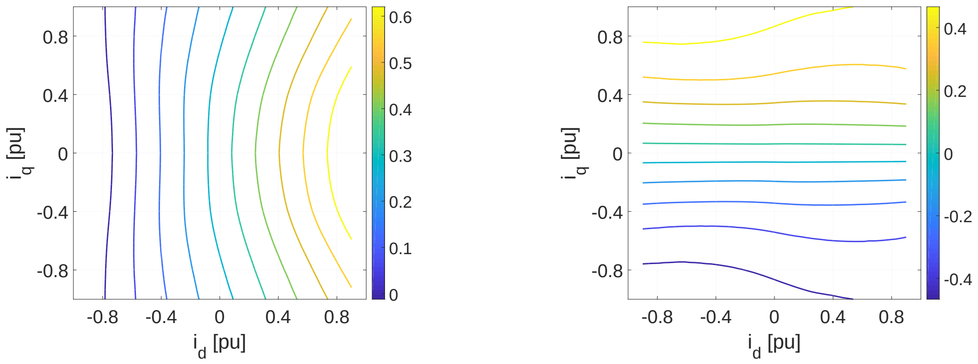

(c) Contour plot of ψ_d **(d)** Contour plot of ψ_q

Figure 2.3: Plots of flux linkages ψ_d and ψ_q

This thesis focuses on modelling the PMSM based on currents dependent flux linkages in the dq coordinate system, thus the variation of temperature T is not included in the analysis. A more accurate model of the PMSM, compared to the one based on fixed inductances, is derived in the following the sections.

Since the flux linkages ψ_d, ψ_q are functions of i_d, i_q, the derivative part can be written as a Jacobian matrix:

$$\begin{gathered}
\begin{cases}
\frac{d\psi_d}{dt} = \frac{\partial \psi_d}{\partial i_d}\frac{di_d}{dt} + \frac{\partial \psi_d}{\partial i_q}\frac{di_q}{dt} \\
\frac{d\psi_q}{dt} = \frac{\partial \psi_q}{\partial i_d}\frac{di_d}{dt} + \frac{\partial \psi_q}{\partial i_q}\frac{di_q}{dt}
\end{cases} \\
\mathbf{J}_\psi = \begin{bmatrix} \frac{\partial \psi_d}{\partial i_d} & \frac{\partial \psi_d}{\partial i_q} \\ \frac{\partial \psi_q}{\partial i_d} & \frac{\partial \psi_q}{\partial i_q} \end{bmatrix}
\end{gathered} \tag{2.10}$$

The 4 partial derivative items represent the physical meaning 'partial inductances', and they can be furthermore classified by d- and q-axis self inductances or mutual inductances[10]. These values can be derived by applying finite-difference method to the flux linkages LUTs.

For simplification, inductance symbols $L_{dd}, L_{dq}, L_{qd}, L_{qq}$ (2.11) are used to represent the 4 partial derivative items. Figure 2.4 shows the mesh plots of the four partial inductances.

$$\begin{array}{ll} L_{dd} = \frac{\partial \psi_d(i_d,i_q)}{\partial i_d} & L_{dq} = \frac{\partial \psi_d(i_d,i_q)}{\partial i_q} \\ L_{qd} = \frac{\partial \psi_q(i_d,i_q)}{\partial i_d} & L_{qq} = \frac{\partial \psi_q(i_d,i_q)}{\partial i_q} \end{array} \tag{2.11}$$

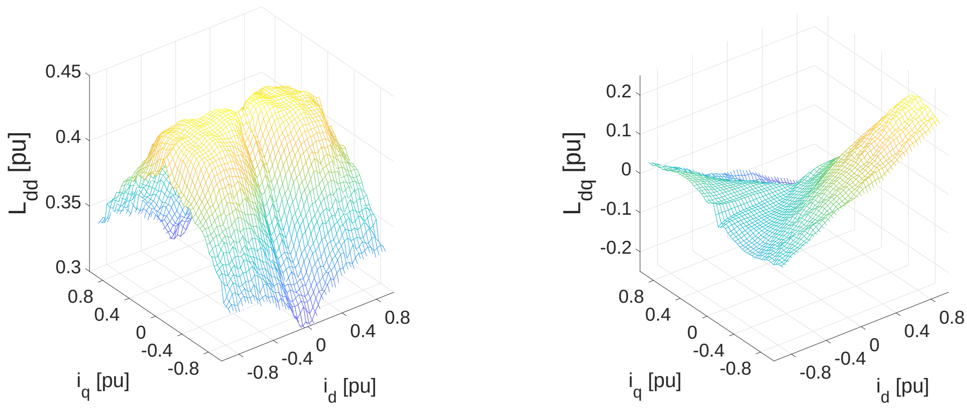

(a) Mesh plot of L_{dd} **(b)** Mesh plot of L_{dq}

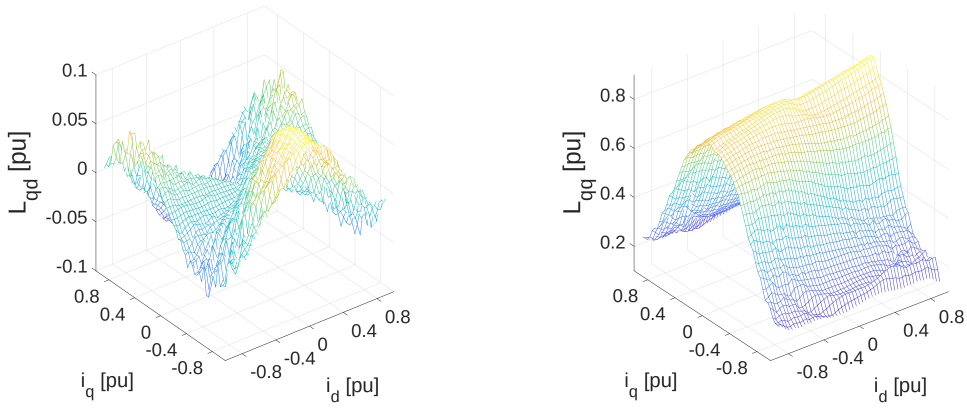

(c) Mesh plot of L_{qd} **(d)** Mesh plot of L_{qq}

Figure 2.4: Mesh plots of the four partial inductances

This more accurate electrical state-space equation of the PMSM can be derived by combining (2.7), (2.10) and (2.11),

$$\mathbf{J}_{\psi} \begin{bmatrix} \dot{i}_d \\ \dot{i}_q \end{bmatrix} = \begin{bmatrix} \frac{\partial \psi_d}{\partial i_d} & \frac{\partial \psi_d}{\partial i_q} \\ \frac{\partial \psi_q}{\partial i_d} & \frac{\partial \psi_q}{\partial i_q} \end{bmatrix} \begin{bmatrix} \dot{i}_d \\ \dot{i}_q \end{bmatrix} = \begin{bmatrix} -R_s & 0 \\ 0 & -R_s \end{bmatrix} \begin{bmatrix} i_d \\ i_q \end{bmatrix} + \begin{bmatrix} 1 & 0 \\ 0 & 1 \end{bmatrix} \begin{bmatrix} u_d \\ u_q \end{bmatrix} + \begin{bmatrix} \omega\psi_q \\ -\omega\psi_d \end{bmatrix} \tag{2.12}$$

The Jacobian matrix $\mathbf{J}_{\psi}$ varies with respect to i_d and i_q, therefore, it is a time-variant non-linear state-space model. Since the self partial inductances L_{dd} and L_{qq}

are always greater than the mutual inductances L_{dq} and L_{qd}, the determinant of Jacobian matrix $|\mathbf{J}_\psi|$ is always greater than 0 (as illustrated in Figure 2.5), which means $\mathbf{J}_\psi$ is invertible at any operation point.

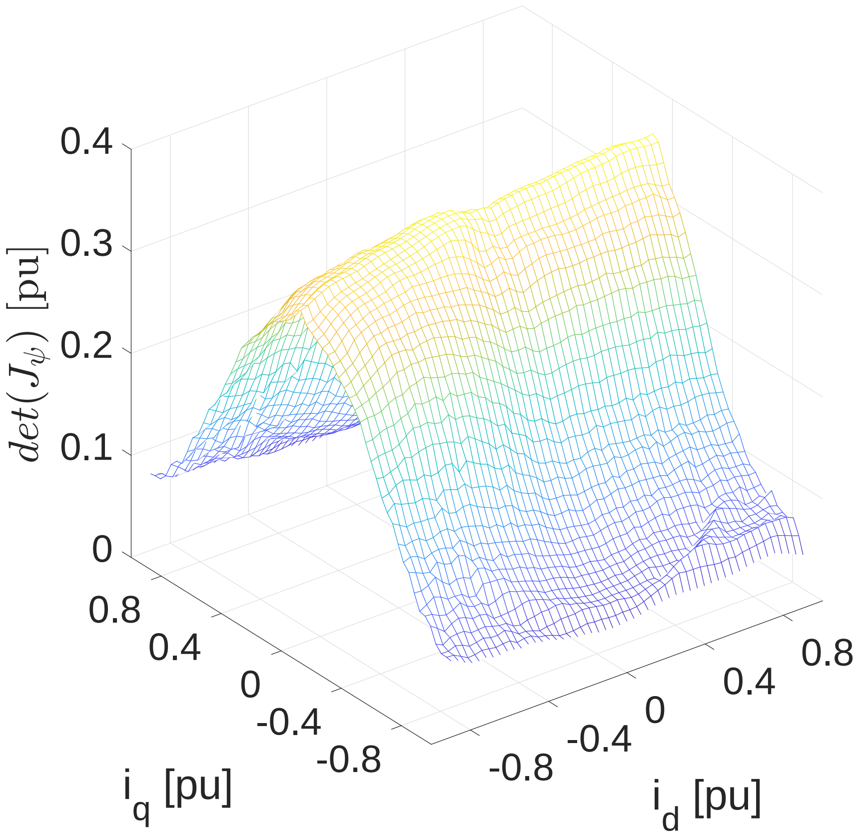

Figure 2.5: Determinant of matrix $\mathbf{J}_\psi$

2. Mechanical equations

The electromagnetic torque equation can be written as

$$T_{em} = \frac{3}{2} n_p (\psi_d i_q - \psi_q i_d) \tag{2.13}$$

where n_p represents the pole pairs of the PMSM.

The relation between the mechanical and electrical angle speed and angle can be written as

$$\begin{cases} \omega_r = n_p \Omega_r \\ \theta_r = n_p \Theta_r \end{cases} \tag{2.14}$$

The mechanical state-space equation of the PMSM can be written as

$$\frac{d\Omega_r}{dt} = -\frac{B_M}{J_M}\Omega_r + \frac{1}{J_M}(T_{em} - T_L) \tag{2.15}$$

$$\frac{d\Theta_r}{dt} = \Omega_r \tag{2.16}$$

where J_M is the inertia constant, B_M is the friction constant and T_L is the load torque.

2.2 Control strategies of the PMSM under various operation conditions

The operation condition, in terms of current and voltage, is for the PMSM highly dependent on the rotational speed, since the back electromagnetic force (back-EMF) $(-\omega_r \psi_q, \omega_r \psi_d)$ is proportional to the speed ω_r. To handle the situation when the induced voltage exceeds the voltage limit of the inverter, which would cause the generated torque to decease, a Field Weakening (FW) strategy needs to be applied in order to extend the speed range of the machine.

At low speed, there are two common ways to control the PMSM:

1. $i_d = 0$ control strategy
As can be seen from (2.13), when $i_d = 0$, $T_{em} = \frac{3}{2} n_p \psi_d i_q$. For the standard modelling method, flux linkages is represented by (2.8). In addition, without a negative d-axis current injected into the PMSM, ψ_d can be regarded as a constant magnetic flux linkage Ψ_m. Therefore, for T_{em}, the only parameter that needs to be controlled is i_q.

2. Maximum Torque Per Ampere (MTPA) control strategy
The feature of this scheme is that the PMSM can produce the required torque with the lowest current. Compared to the first case, a larger maximum torque can be achieved and heating losses will be reduced.

Different from the standard featured current states trajectories (MTPA, FW, etc.) as derived from the standard PMSM model (2.9) which neglect the influence of magnetic saturation and cross-coupling [8][9], the following current states trajectory derivations are based on the more accurate PMSM model (2.12) using the i_d, i_q based variables $\psi_d, \psi_q, L_{dd}, L_{dq}, L_{qd}, L_{qq}$. The current states trajectories of the standard PMSM model will be included for comparison.

2.2.1 Maximum Torque Per Ampere control strategy

2.2.1.1 MTPA trajectory

The method of Lagrangian function with a Lagrange multiplier λ can be introduced to help find the local maximum or minimum point of a function $f(x, y)$ which subjects to the equality constraints $g(x, y) = c$, where c is a constant value[13].

$$\mathcal{L}(x, y, \lambda) = f(x, y) + \lambda \cdot (g(x, y) - c) \tag{2.17}$$

For the MTPA control strategy, at a given torque value, the optimal point (i_d, i_q) which produces the minimum current amplitude $\sqrt{i_d^2 + i_q^2}$ should be derived so that the value of 'torque per ampere' is the maximum. Equation (2.18) is the function which represents the square of current amplitude (for calculation simplicity). Equation (2.19) defines the equality constraints, i_d, i_q should be restricted by (2.13) when giving a reference torque T_{ref}. By introducing the Lagrange multiplier λ, the Lagrange function can be defined as (2.20). The derivation process is listed below.

$$f(i_d, i_q) = i_d^2 + i_q^2 \tag{2.18}$$

$$g(i_d, i_q) = \frac{3}{2} n_p (\psi_d i_q - \psi_q i_d) = T_{ref} \tag{2.19}$$

$$F(i_d, i_q, \lambda) = f(i_d, i_q) + \lambda (T_{ref} - g(i_d, i_q)) \tag{2.20}$$

$$\begin{cases} \frac{\partial F}{\partial i_d} = 2i_d + \frac{3}{2} n_p \lambda (-\frac{\partial \psi_d}{\partial i_d} i_q + \frac{\partial \psi_q}{\partial i_d} i_d + \psi_q) = 0 \\ \frac{\partial F}{\partial i_q} = 2i_q + \frac{3}{2} n_p \lambda (-\frac{\partial \psi_d}{\partial i_q} i_q - \psi_d + \frac{\partial \psi_q}{\partial i_q} i_d) = 0 \\ \frac{\partial F}{\partial \lambda} = T_{ref} - \frac{3}{2} n_p (\psi_d i_q - \psi_q i_d) = 0 \end{cases} \tag{2.21}$$

By Combining the first and second equations from (2.21), the MTPA trajectory equation in this thesis can de described as

$$L_{qq} i_d^2 + L_{dd} i_q^2 - (L_{dq} + L_{qd}) i_d i_q - \psi_d i_d - \psi_q i_q = 0 \tag{2.22}$$

For comparison, the MTPA trajectory of the standard PMSM model is formulated as

$$i_d + \frac{L_d - L_q}{\Psi_m} \left(i_d^2 - i_q^2 \right) = 0 \tag{2.23}$$

As can be seen in Figure 2.6, the dashed blue lines specify the current combinations at different reference torque levels T_{ref}. The dashed green line represents the MTPA trajectory derived from the standard model (2.23), while the solid green line describes the MTPA trajectory according to (2.22) calculated. When the torque reference is low, the two derived MTPA trajectories are similar, but as the torque reference rises, they start to deviate. For the standard PMSM model, its MTPA trajectory function (2.23) is a hyperbola. The MTPA trajectory calculated from (2.22) is quasi hyperbolic, since the magnetic saturation and the cross-coupling effects are taken into consideration. For the other operation trajectories in the following paragraph (Field Weakening, MTPV), the trajectories which are derived from the standard PMSM model (2.9) and the more accurate PMSM model (2.12) are almost identical, thus the comparisons between these trajectories will not be discussed.

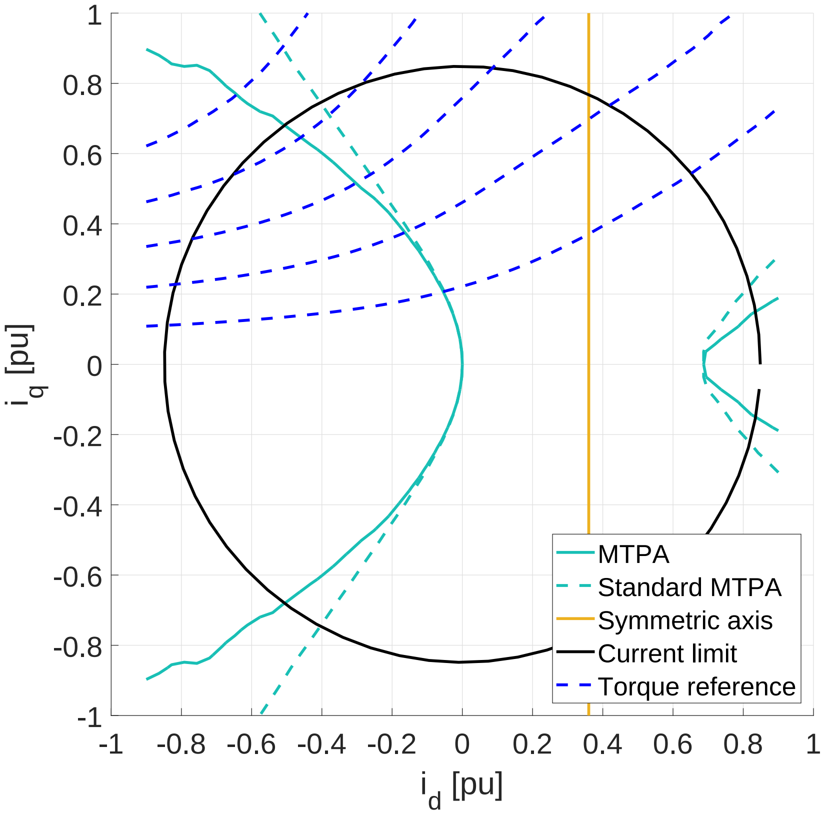

Figure 2.6: Comparison of two MTPA trajectories

The MTPA trajectory has two axisymmetric curves. Usually, the PMSM should operate at the left half axis. For (2.23), the symmetric axis of a hyperbola is

$$i_d = \frac{-\Psi_m}{2(L_d - L_q)} \tag{2.24}$$

For the quasi hyperbolic MTPA function (2.22), the symmetric axis cannot be derived directly. By using (2.22) and setting $i_q = 0$, the following equation can be derived

$$\psi_d(i_d, 0)i_d - L_{qq}(i_d, 0)i_d^2 = 0 \tag{2.25}$$

The solution is $i_{d1} = 0$ and $i_{d2} = \frac{\psi_d(i_d,0)}{L_{qq}(i_d,0)}$. It can be roughly assumed that the symmetric axis is the middle point, thus the operation region for the d-axis current is

$$i_d < \frac{i_{d1} + i_{d2}}{2} \tag{2.26}$$

2.2.1.2 Current limit

Due to thermal constraints of the inverter, the semi-conductor chips are heated up very fast, the inverter phase current should be restricted under a maximum value. This means that the MTPA control strategy has a limited operation region. When the current reaches its boundary I_{max}, the PMSM can generate the maximum electromagnetic torque.

$$\sqrt{i_d^2 + i_q^2} \leqslant I_{max} \tag{2.27}$$

2.2.2 Field Weakening control strategy

2.2.2.1 Voltage limit

For (2.7), by neglecting the stator resistance and assuming steady-state operation, the voltage equations can be approximated as

$$\begin{cases} u_d \approx -\omega_r \psi_q \\ u_q \approx +\omega_r \psi_d \end{cases} \tag{2.28}$$

In order to control the PMSM at high speed, it is necessary to keep the voltage amplitude below the maximum input voltage U_{max}, which is set by the dc-link of the inverter.

$$\sqrt{u_d^2 + u_q^2} = \omega_r \sqrt{\psi_d^2 + \psi_q^2} \leqslant U_{max} \tag{2.29}$$

For low speeds, where the voltage amplitude is below the maximum input voltage, current combinations are chosen along the MTPA trajectory for the different torque references. As the speed ω_r increases, the flux amplitude $\sqrt{\psi_d^2 + \psi_q^2}$ will be reduced to meet the voltage limit restriction of the inverter. For the standard PMSM model, since ψ_d, ψ_q can be formulated as (2.8), where the corresponding field weakening equation can be defined as (2.30), the flux amplitude can be decreased by applying lower values of i_d, i_q, which is the same way for (2.29) to reduce the flux amplitude. This is the principle how the field weakening control strategy works.

$$\sqrt{u_d^2 + u_q^2} = \omega_r \sqrt{(L_d i_d + \Psi_m)^2 + (L_q i_q)^2} \leqslant U_{max} \tag{2.30}$$

For the standard PMSM model, the field weakening trajectory (2.30) is an ellipse with its center at the point ($-\Psi_m/L_d, 0$). As the electrical speed ω_r goes up, the 'diameter' of the ellipse shrinks. As can be seen in Figure 2.7, the trajectories derived from (2.29) using the i_d, i_q based flux LUTs are shrinking like quasi ellipses, and the converging point is labelled with O.

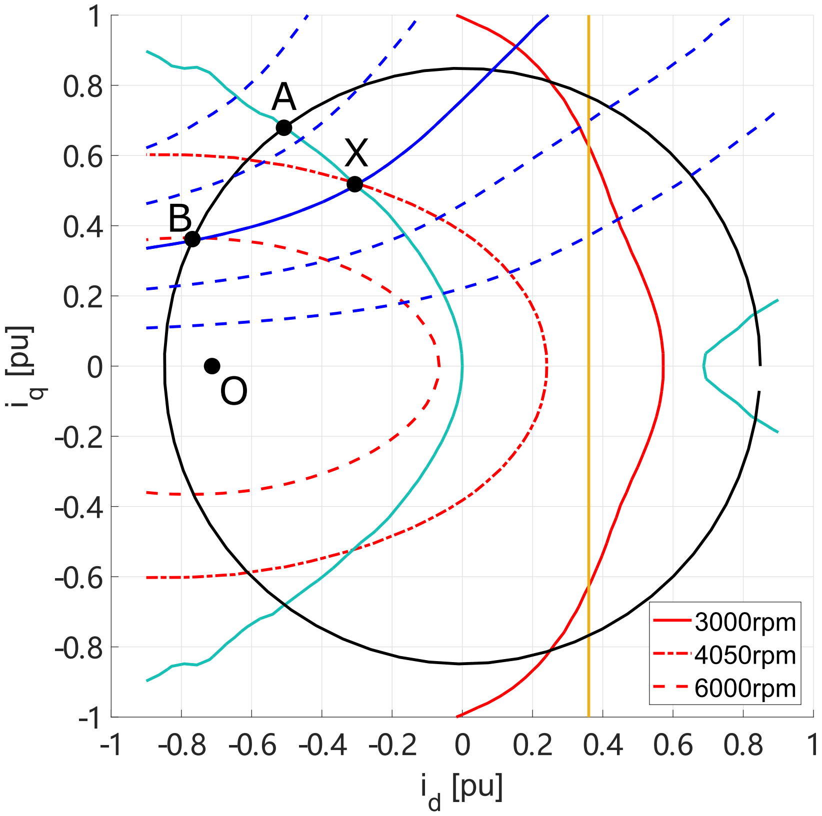

Figure 2.7: Field weakening (voltage limit) trajectories at different speeds

When the speed ω_r is low, the intersection point A between the MTPA and the current limit trajectories is the boundary that the MTPA control strategy can reach. In Figure 2.7, three red curves indicate the shrinking field weakening trajectories at different rotating speeds. The solid blue curve represents the desired reference torque of 0.75 [pu] for the PMSM.

(1) When the speed is 3000 [rpm], the shrinking voltage limit ellipse has no effect on the current states, the PMSM model can operate along the MTPA trajectory till the current limit boundary.

(2) When the speed is 4050 [rpm], the MTPA trajectory has been cut by the shrinking voltage limit ellipse at point X, this means that beyond point X (speed exceeds 4050 [rpm]), the MTPA control strategy cannot function any more, and the field weakening control strategy should take place for further operation. The current states need to evolve along the 0.75 [pu] reference torque curve.

(3) When the speed is 6000 [rpm], the evolving current states reach the current limit boundary at point B. Therefore, 6000 [rpm] is the highest speed this PMSM can achieve when the desired generated torque is 0.75 [pu]. Since the 6000 [rpm] voltage limit ellipse is completely on the left side of the MTPA trajectory, if the PMSM

starts its operation at this speed (first speeded up by the external load), the field weakening control strategy will be applied directly.

(4) As the torque reference signal goes up, the current states jump from zero point to point X along the MTPA trajectory. Assuming that the speed reference signal begins to increase at the same time, the current states stay at point X before the speed comes to 4050 [rpm]. If the speed keeps rising (field weakening ellipse keeps shrinking), the current states will go along the solid blue 0.75 [pu] torque reference trajectory. At the intersection point B between the torque reference and the current limit, the PMSM will reach its highest speed, 6000 [rpm], where the generated torque still can meet the torque reference.

This means that, for a constant torque reference, the field weakening control strategy enables the PMSM to achieve a higher rotational speed when compared to the MTPA control strategy.

2.2.2.2 Maximum Torque Per Volt control strategy

If it is assumed that the reference torque tracking is a weak constraint for the PMSM control, this means that exceeding the speed is allowed which will bring a sacrifice of the electromagnetic torque generated by the PMSM. In order to achieve infinite speed PMSM control, Maximum Torque Per Volt (MTPV) control strategy is introduced to improve the high speed control performance[11].

For the MTPV control strategy, at a given torque value, the optimal point (i_d, i_q) which produces the minimum voltage amplitude $\sqrt{u_d^2 + u_q^2}$ should be derived so that the value of 'torque per volt' is maximized. Equation (2.31) is the function which represents the square of voltage amplitude (same voltage approximation as (2.28)). Equation (2.32) defines the equality constraints, i_d, i_q which should be restricted by (2.13) when giving a reference torque T_{ref}. By introducing the Lagrange multiplier λ, the Lagrange function can be defined as (2.33). The derivation process is listed below.

$$f'(u_d, u_q) = u_d^2 + u_q^2 \approx \omega_r^2(\psi_d^2 + \psi_q^2) \tag{2.31}$$

$$g(i_d, i_q) = \frac{3}{2} n_p(\psi_d i_q - \psi_q i_d) = T_{ref} \tag{2.32}$$

$$F'(i_d, i_q, \lambda) = f'(i_d, i_q) + \lambda(T_{ref} - g(i_d, i_q)) \tag{2.33}$$

$$\begin{cases} \frac{\partial F}{\partial i_d} = 2\omega_r^2(\frac{\partial \psi_d}{\partial i_d}\psi_d + \frac{\partial \psi_q}{\partial i_d}\psi_q) + \frac{3}{2}n_p\lambda(-\frac{\partial \psi_d}{\partial i_d}i_q + \frac{\partial \psi_q}{\partial i_d}i_d + \psi_q) = 0 \\ \frac{\partial F}{\partial i_q} = 2\omega_r^2(\frac{\partial \psi_d}{\partial i_q}\psi_d + \frac{\partial \psi_q}{\partial i_q}\psi_q) + \frac{3}{2}n_p\lambda(-\frac{\partial \psi_d}{\partial i_q}i_q - \psi_d + \frac{\partial \psi_q}{\partial i_q}i_d) = 0 \\ \frac{\partial F}{\partial \lambda} = T_{ref} - \frac{3}{2}n_p(\psi_d i_q - \psi_q i_d) = 0 \end{cases} \tag{2.34}$$

Combine the first and second equations from (2.34), the MTPV equation can be written as

$$\frac{\psi_d^2}{L_{qq}} + \frac{\psi_q^2}{L_{dd}} + \frac{L_{dq}+L_{qd}}{L_{dd}L_{qq}}\psi_d\psi_q - (1 - \frac{L_{dq}L_{qd}}{L_{dd}L_{qq}})(\psi_d i_d + \psi_q i_q) = 0 \tag{2.35}$$

Since L_{dd} and L_{qq} are always positive, it is feasible to put them in the denominator.

For comparison, the MTPV trajectory of the standard PMSM model is formulated as

$$\frac{\Psi_m^2}{L_q} + \Psi_m\left(2\frac{L_d}{L_q} - 1\right) i_d + L_d\left(\frac{L_d}{L_q} - 1\right) i_d^2 + L_q\left(\frac{L_q}{L_d} - 1\right) i_q^2 = 0 \tag{2.36}$$

For the standard PMSM model, its MTPV trajectory function (2.36) is a hyperbola. As can be seen in Figure 2.8, the MTPV trajectory calculated from (2.35) is quasi hyperbolic.

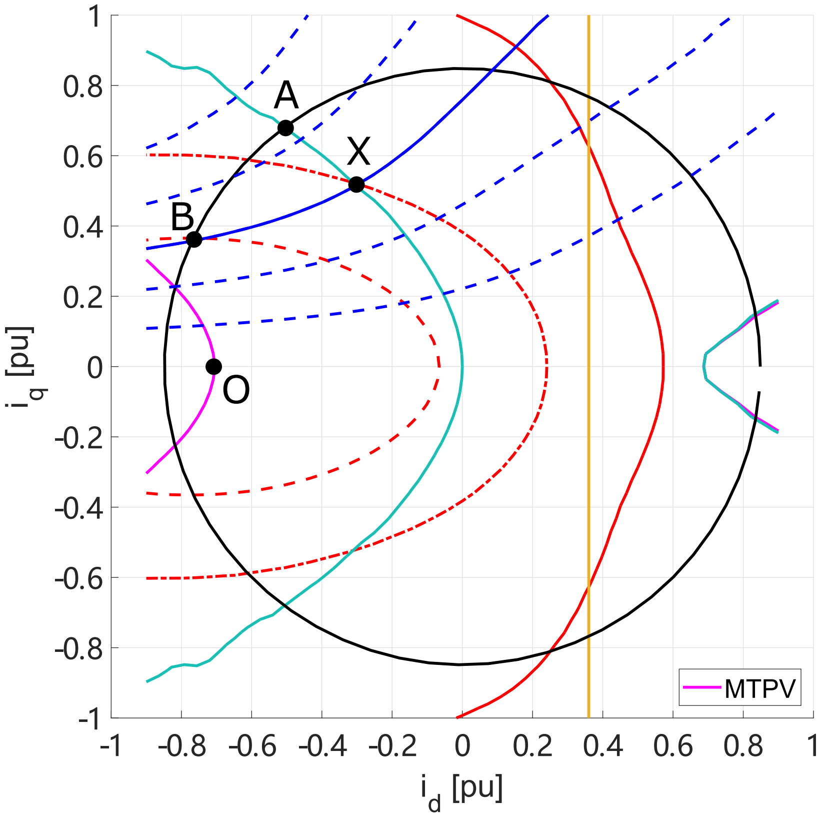

Figure 2.8: MTPV trajectory

Similar to the principle of MTPA, where the MTPA trajectory is composed by the set of tangent points between different torque reference curves and their corresponding tangent current amplitude circles, the MTPV trajectory is composed by the set of tangent points between different torque reference curves and their corresponding tangent voltage amplitude (field weakening) ellipses. Therefore, the MTPV trajectory is always orthogonal to the constant torque lines and it intersects with the shrinking field weakening ellipse center O. On the other hand, for a given speed (refers to a given voltage limit ellipse), the MTPV trajectory helps specify the current operating point where the PMSM can generate the maximum electromagnetic torque T_{em}. This is how the MTPV control strategy helps to achieve high speed operation while maximizing the generated torque as much as possible.

One thing that needs to be mentioned, is that the MTPV control strategy can be used to achieve infinite speed PMSM control only if the shrinking voltage limit ellipse center O is inside the current limit circle. This can be satisfied if an inverter with sufficiently high current rating is equipped and the PMSM is able to handle this current overload.

2.3 Introduction of the Two-Level Voltage Source Inverter

2.3.1 Switching states of the two-level voltage source inverter

Two-level Voltage Source Inverters (VSI) has been widely used in different electrical applications for its simple configuration and proven technology. Figure 2.9 shows the topology of a two-level VSI.

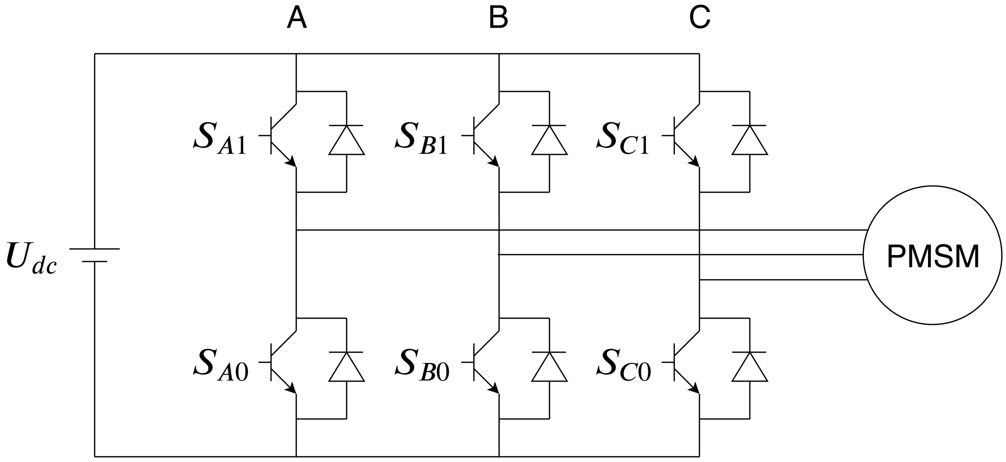

Figure 2.9: Two-level voltage source inverter

A two-level VSI has three phase legs (A,B,C) and a pair of two switches (S_{X1},S_{X0}) for each phase leg. For the PMSM operation in this thesis, one of the S_{X1},S_{X0} must be turned on and the other switch must be turned off. For convenience, logical values 0 or 1 are used to help define the switching state for each phase leg, where 1 represents S_{X1} is on and S_{X0} is off, 0 represents S_{X0} is on and S_{X1} is off. Therefore, a total of $2^3 = 8$ switching states ($S_A S_B S_C$) can be generated by the two-level VSI, they are (000),(001),(010),(011),(100),(101),(110),(111). Figure 2.10 illustrates the relation between the switching states $(S_A S_B S_C)$ and the $\alpha\beta$ coordinate system.

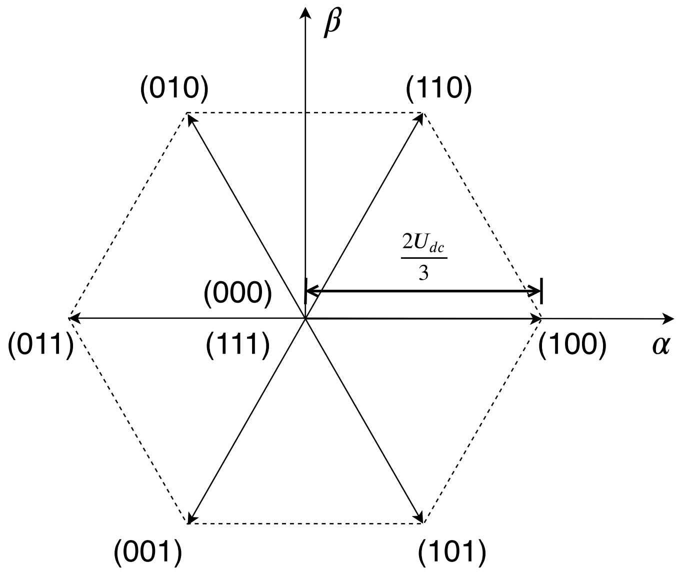

Figure 2.10: Relation between the switching states $(S_A S_B S_C)$ and the $\alpha\beta$ coordinate system

In order to have a convenient regulation for the voltage vectors of the two-level VSI, the switching states need to be transformed into the $\alpha\beta$ coordinates. The phase angle difference between each phase leg is $2\pi/3$, the coordinate transformation method can be derived as

$$\begin{gathered} u_s = \tfrac{2}{3} U_{dc} \left(S_A \, e^{j0} + S_B \, e^{j2\pi/3} + S_C \, e^{j4\pi/3} \right) \\ \begin{bmatrix} U_\alpha \\ U_\beta \end{bmatrix} = \tfrac{2}{3} U_{dc} \begin{bmatrix} 1 & -\frac{1}{2} & -\frac{1}{2} \\ 0 & \frac{\sqrt{3}}{2} & -\frac{\sqrt{3}}{2} \end{bmatrix} \begin{bmatrix} S_A \\ S_B \\ S_C \end{bmatrix} \end{gathered} \tag{2.37}$$

where U_{dc} is the DC-link voltage of the two-level VSI and the amplitude invariant factor $C_{3s/2s} = \frac{2}{3}$ is used.

2.3.2 Space vector pulse width modulation scheme

Space Vector Pulse Width Modulation (SVPWM) is a commonly used modulation scheme for the field oriented control of the PMSM[18]. The two-level VSI block of the benchmark system (introduced in Chapter 4) generates the required voltage vectors from the PI controller by using the SVPWM scheme. As can be seen in Figure 2.11, a reference voltage vector U_{ref} can be derived by taking the average in one switching interval T_{sw} as (2.38) shows. $U_{dc}/\sqrt{3}$ is the rated output voltage (radius of the inscribed circle) based on the maximum circular SVPWM scheme.

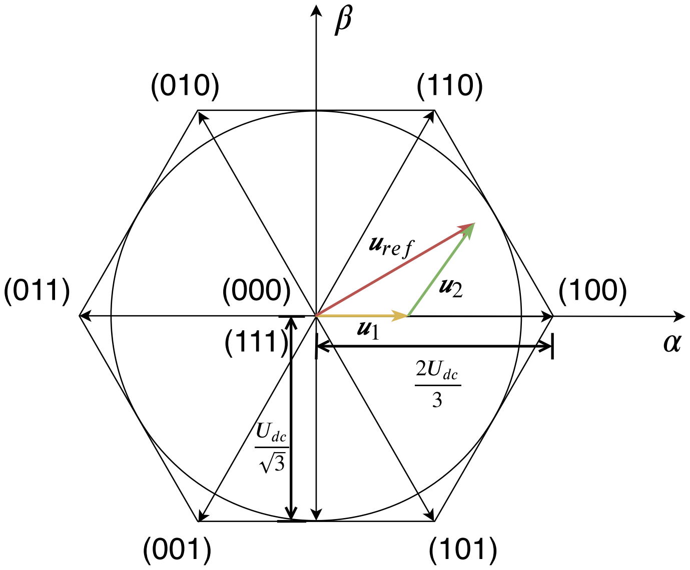

Figure 2.11: Voltage vectors under SVPWM scheme

$$\begin{gathered}
T_{(100)} = \left|\frac{\boldsymbol{u}_1}{\boldsymbol{u}_{(100)}}\right| T_{sw} \\
T_{(110)} = \left|\frac{\boldsymbol{u}_2}{\boldsymbol{u}_{(110)}}\right| T_{sw} \\
T_{(000)} = T_{sw} - (T_{(100)} + T_{(110)}) \\
\boldsymbol{u}_{ref} = \boldsymbol{u}_{(100)} T_{(100)} + \boldsymbol{u}_{(110)} T_{(110)} + \boldsymbol{u}_{(000)} T_{(000)}
\end{gathered} \tag{2.38}$$

Compared to using the eight switching states directly, the SVPWM scheme enables the two-level VSI to generate more selections of the required voltage vector by the method of averaging. In addition, the SVPWM scheme helps to reduce the total harmonic distortion and the current and torque ripples.

3

Method

3.1 Discretization of the PMSM model

In order to realize an FCS-MPC control algorithm for the PMSM, a discretized PMSM model is needed to predict the states of the PMSM over a certain time horizon (>=1).

Usually, there are two methods to realize the discretization of a state-space model: The Forward Euler method and Zero-Order Hold (ZOH) method. The derivation of the discretization starts from the continuous PMSM model (2.12), a general symbolized equation of (2.12) can be written as

$$J\dot{x}(t) = Ax(t) + Bu(t) + E \tag{3.1}$$

where

$$\begin{array}{lll} J = \mathbf{J}_\psi = \begin{bmatrix} L_{dd} & L_{dq} \\ L_{qd} & L_{qq} \end{bmatrix} & x = \begin{bmatrix} i_d \\ i_q \end{bmatrix} & u = \begin{bmatrix} u_d \\ u_q \end{bmatrix} \\ A = \begin{bmatrix} -R_s & 0 \\ 0 & -R_s \end{bmatrix} & B = \begin{bmatrix} 1 & 0 \\ 0 & 1 \end{bmatrix} & E = \begin{bmatrix} \omega_r \psi_q \\ -\omega_r \psi_d \end{bmatrix} \end{array} \tag{3.2}$$

By setting a sampling time T_s which is relatively small compared to the time constant of the PMSM, it can be regarded that J, A, E are constant values during each sampling interval. Also, as described in Chapter 2, J is invertible at any operation point.

1. Forward Euler method

For the Forward Euler method, $u(t)$, $x(t)$ and $\dot{x}(t)$ can be transformed to $u(k)$, $x(k)$ and $(x(k+1) - x(k)/T_s)$ respectively in discretized form. The derivation process is shown as below.

$$\begin{aligned} J\frac{x(k+1) - x(k)}{T_s} &= Ax(k) + Bu(k) + E(k) \\ x(k+1) &= J^{-1}T_s(Ax(k) + Bu(k) + E) + x(k) \\ &= J^{-1}[AT_s x(k) + BT_s u(k) + ET_s + Jx(k)] \\ &= J^{-1}(AT_s + J)\, x(k) + J^{-1}BT_s\, u(k) + J^{-1}ET_s \\ &= A_d(k)\, x(k) + B_d(k)\, u(k) + E_d(k) \end{aligned} \tag{3.3}$$

Usually, the prediction errors of the Forward Euler method is obvious at low sampling frequency since it is a first order approximation of the system.

2. Zero-Order Hold method
For Zero-Order Hold method, the discretization can be derived by

$$\begin{aligned} x(k+1) &= e^{J^{-1}AT_s}\,x(k) + \int_0^{T_s} e^{J^{-1}A\tau}J^{-1}(Bu(k)+E)\,d\tau \\ &= e^{J^{-1}AT_s}\,x(k) + \int_0^{T_s} e^{J^{-1}A\tau}d\tau\,J^{-1}Bu(k) + \int_0^{T_s} e^{J^{-1}A\tau}d\tau\,J^{-1}E \\ &= A_d(k)\,x(k) + B_d(k)\,u(k) + E_d(k) \end{aligned} \tag{3.4}$$

The matrix exponential term $e^{J^{-1}AT_s}$ can be computed with the help of high order approximation or Jordan normal form[14].

3.2 Introduction of the Model Predictive Control

For electric drives, the conventional control methods are linear control with the help of certain modulation schemes and non-linear control in the form of hysteresis bounds[15]. But the drawback of these methods is that they cannot perform well when it comes to the physical constraints and parameter variations, such as limited current amplitude and its slew rate, variations of resistance, flux at elevated temperature and so on. To control such constrained systems, the model predictive control method has been applied into the area of electric drives and power electronics[16]. Model Predictive Control (MPC) method was introduced during the 80s in chemical and petroleum industry. The main objective was to increase the product quality and reduce losses while respecting all operational limits. With the rapid development of embedded processing hardware, the realization of electric drives control based on the MPC method has become more mature.

In order to utilize the MPC method, a more accurate discrete dynamic model of the electric drive is needed to predict its future states. The number of the predicted future time steps is defined as prediction horizon N. A control objective is formulated as an optimization problem which it minimizes a certain cost function, which is typically a convex function of predicted system states x and control input u, over a prediction horizon N using control input as an optimization variable while respecting system dynamic and static constraints. This results in an optimal control sequence that steers the system towards the desired target/trajectory. MPC solves this constrained optimal control problem in a receding horizon fashion (i.e., fixing origin of time axis at current step and then predicting future evolution of system states over a short horizon). The main advantage of MPC is that it can handle constraints systematically and solve infinite horizon full optimal control problem by solving finite horizon optimal control problems in a receding horizon fashion.

Generally, depending on how to formulate the input voltage vectors for states prediction, MPC can be classified into two different types, Continuous Control Set

MPC (CCS-MPC) and Finite Control Set MPC (FCS-MPC)[17]. For CCS-MPC, a continuous set of the voltage vectors is evaluated in the cost function, the optimal voltage vector can be generated with the help of a SVPWM scheme inverter. For FCS-MPC, a finite set of the voltage vectors (e.g. eight switching states of a two-level VSI) is applied into the cost function, the optimal voltage vector is the one which minimizes the cost function. SVPWM scheme is not needed under this control method. In this thesis, FCS-MPC scheme is utilized to realize the PMSM operation. Figure 3.1 briefly shows the execution process of FCS-MPC and details are discussed in the following section.

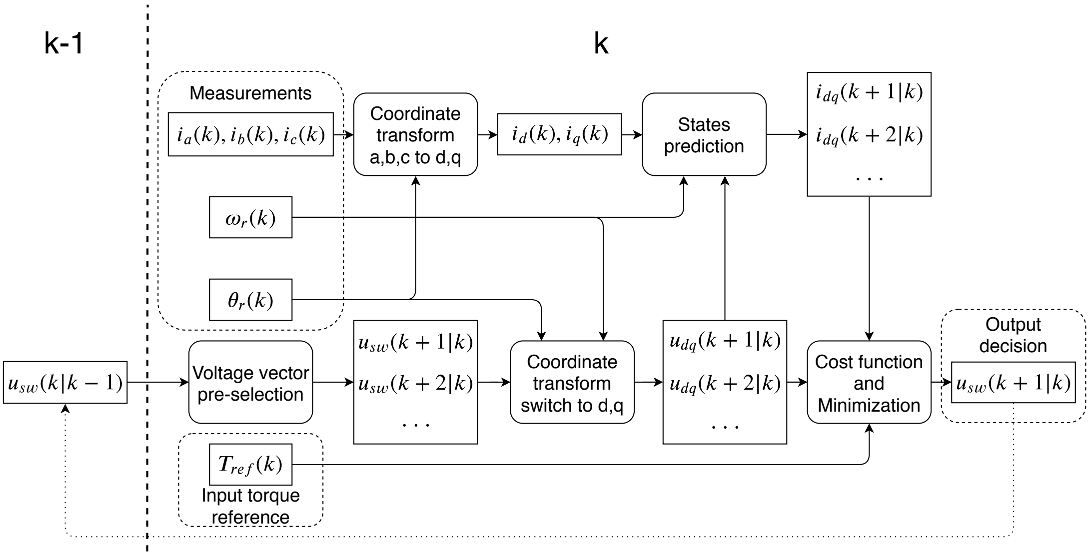

Figure 3.1: Execution process of FCS-MPC

3.3 Execution of the FCS-MPC algorithm

3.3.1 Measurement

Since this thesis focuses on how to implement the control algorithm in a time-variant state-space PMSM model, the influence of the measured current noise is neglected for simplicity. The FCS-MPC algorithm starts from taking in the measured parameters of the three phase currents $i_a(k), i_b(k), i_c(k)$, electrical rotating speed $\omega_r(k)$, electrical angle $\theta_r(k)$ and torque reference $T_{ref}(k)$ at the current time step k. The three phase currents need to be transformed to dq coordinate currents $i_d(k), i_q(k)$ for the implementation of FCS-MPC control.

3.3.2 Prediction

3.3.2.1 Voltage vector pre-selection

As mentioned in Chapter 2, eight switching states in total can be generated by a two-level VSI. In this thesis, in order to reduce the switching losses, it is assumed that between each two sampling instances, at most one of the three inverter phase legs can change its switching state. Therefore, not all the eight switching states can be reachable in one time step.

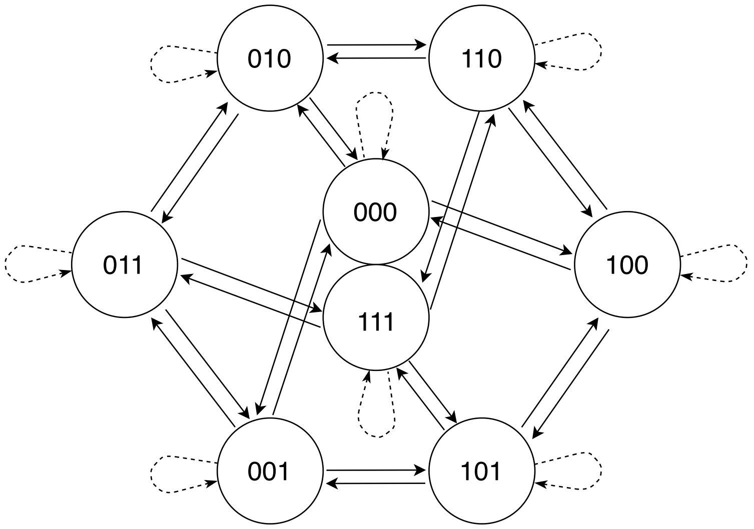

Figure 3.2: Pre-selection of switching states

Figure 3.2 presents the possible selections of each switching state. The different arrangements of the logical values 0 or 1 represent the current switching states ($S_A S_B S_C$) for all the three phase legs A,B,C. The arrow indicates that the switching state change can be achieved during one sampling instance. It can be regarded that for each switching state, four possible switching states can be reached at the next time step under the assumption that only one phase leg can change its switching state. Logical operator Exclusive OR (XOR) is introduced to help realize such switch selection scheme.

Table 3.1: XOR truth table

A	B	A XOR B
0	0	0
0	1	1
1	0	1
1	1	0

It can be summed that for a logical value S, S XOR 1 equals to $\bar{S}$, S XOR 0 equals to S. Since the switching states for each phase leg are defined in logical values (0 or 1), applying 'XOR 1' to the phase switching state can be regarded as a state change, while applying 'XOR 0' can be regarded as a state maintenance. Matrix form of XOR operator (3.5) is utilized to derive the four possible switching states at next time step.

$$\begin{bmatrix} \mathrm{S_A} & \mathrm{S_A} & \mathrm{S_A} & \mathrm{S_A} \\ \mathrm{S_B} & \mathrm{S_B} & \mathrm{S_B} & \mathrm{S_B} \\ \mathrm{S_C} & \mathrm{S_C} & \mathrm{S_C} & \mathrm{S_C} \end{bmatrix} \mathrm{XOR} \begin{bmatrix} 1 & 0 & 0 & 0 \\ 0 & 1 & 0 & 0 \\ 0 & 0 & 1 & 0 \end{bmatrix} = \begin{bmatrix} \overline{\mathrm{S_A}} & \mathrm{S_A} & \mathrm{S_A} & \mathrm{S_A} \\ \mathrm{S_B} & \overline{\mathrm{S_B}} & \mathrm{S_B} & \mathrm{S_B} \\ \mathrm{S_C} & \mathrm{S_C} & \overline{\mathrm{S_C}} & \mathrm{S_C} \end{bmatrix} \tag{3.5}$$

Thus the voltage vector pre-selection function over the prediction horizon N can be written as

$$\begin{gathered} U_{sw}(k+1) = [u_{sw}(k)\ u_{sw}(k)\ u_{sw}(k)\ u_{sw}(k)]\ \mathrm{XOR}\ V_1 \\ U_{sw}(k+2) = [U_{sw}(k+1)\ U_{sw}(k+1)\ U_{sw}(k+1)\ U_{sw}(k+1)]\ \mathrm{XOR}\ V_2 \\ \dots\dots \end{gathered} \tag{3.6}$$

where switch voltage u_{sw} represents the voltage vector in the form of switching state $(S_A\ S_B\ S_C)^T$ and

$$\begin{gathered} V_1 = \begin{bmatrix} 1 & 0 & 0 & 0 \\ 0 & 1 & 0 & 0 \\ 0 & 0 & 1 & 0 \end{bmatrix} \\ V_2 = \begin{bmatrix} 1 & 1 & 1 & 1 & 0 & 0 & 0 & 0 & 0 & 0 & 0 & 0 & 0 & 0 & 0 & 0 \\ 0 & 0 & 0 & 0 & 1 & 1 & 1 & 1 & 0 & 0 & 0 & 0 & 0 & 0 & 0 & 0 \\ 0 & 0 & 0 & 0 & 0 & 0 & 0 & 0 & 1 & 1 & 1 & 1 & 0 & 0 & 0 & 0 \end{bmatrix} \end{gathered} \tag{3.7}$$

Figure 3.3 illustrates an example how the voltage vectors are pre-selected when prediction horizon N=2.

$$u_{sw}(k): \quad \begin{bmatrix} 1 \\ 0 \\ 0 \end{bmatrix}$$

$$U_{sw}(k+1): \quad \begin{bmatrix} 1 & 1 & 1 & 1 \\ 0 & 0 & 0 & 0 \\ 0 & 0 & 0 & 0 \end{bmatrix} XOR \underset{V_1}{\begin{bmatrix} 1 & 0 & 0 & 0 \\ 0 & 1 & 0 & 0 \\ 0 & 0 & 1 & 0 \end{bmatrix}} = \begin{bmatrix} 0 & 1 & 1 & 1 \\ 0 & 1 & 0 & 0 \\ 0 & 0 & 1 & 0 \end{bmatrix}$$

4 repeating

$$U_{sw}(k+1): \quad \begin{bmatrix} 0 & 1 & 1 & 1 \\ 0 & 1 & 0 & 0 \\ 0 & 0 & 1 & 0 \end{bmatrix} \begin{bmatrix} 0 & 1 & 1 & 1 \\ 0 & 1 & 0 & 0 \\ 0 & 0 & 1 & 0 \end{bmatrix} \begin{bmatrix} 0 & 1 & 1 & 1 \\ 0 & 1 & 0 & 0 \\ 0 & 0 & 1 & 0 \end{bmatrix} \begin{bmatrix} 0 & 1 & 1 & 1 \\ 0 & 1 & 0 & 0 \\ 0 & 0 & 1 & 0 \end{bmatrix}$$

$$XOR$$

$$V_2: \quad \begin{bmatrix} 1 & 1 & 1 & 1 \\ 0 & 0 & 0 & 0 \\ 0 & 0 & 0 & 0 \end{bmatrix} \begin{bmatrix} 0 & 0 & 0 & 0 \\ 1 & 1 & 1 & 1 \\ 0 & 0 & 0 & 0 \end{bmatrix} \begin{bmatrix} 0 & 0 & 0 & 0 \\ 0 & 0 & 0 & 0 \\ 1 & 1 & 1 & 1 \end{bmatrix} \begin{bmatrix} 0 & 0 & 0 & 0 \\ 0 & 0 & 0 & 0 \\ 0 & 0 & 0 & 0 \end{bmatrix}$$

$$=$$

$$U_{sw}(k+2): \quad \begin{bmatrix} 1 & 0 & 0 & 0 \\ 0 & 1 & 0 & 0 \\ 0 & 0 & 1 & 0 \end{bmatrix} \begin{bmatrix} 0 & 1 & 1 & 1 \\ 1 & 0 & 1 & 1 \\ 0 & 0 & 1 & 0 \end{bmatrix} \begin{bmatrix} 0 & 1 & 1 & 1 \\ 0 & 1 & 0 & 0 \\ 1 & 1 & 0 & 1 \end{bmatrix} \begin{bmatrix} 0 & 1 & 1 & 1 \\ 0 & 1 & 0 & 0 \\ 0 & 0 & 1 & 0 \end{bmatrix}$$

Figure 3.3: Example of the voltage vector pre-selection

When the prediction horizon N=1, the predicted switch voltage matrix $U_{sw}(k+1)$ contains four possible switching states derived from $u_{sw}(k)$. Therefore, if a higher prediction horizon N is required, the number of the derived voltage vectors in $U_{sw}(k+N)$ equals to 4^N, which means the number of the results that need to be verified in the cost function is 4^N. Also, it can be inferred that the arrangement of the cost function results is aligned with the repeating sequence of $U_{sw}(k+1)$.

In order to quantify the performance of switching losses reduction, the average switch S_{avg} and the average switching frequency f_{avg} of the inverter can be introduced. The average switch S_{avg} is defined as (3.8) which is characterised as the moving average of the total switching state changes during certain intervals.

$$S_{avg}(k) = \frac{\text{sum}(Q_{sw}(k))}{\text{length}(Q_{sw}(k))} \tag{3.8}$$

where $Q_{sw}(k)$ is an array with queue data structure (first in first out), at the beginning of each computation interval, it takes in a logical value of whether the decision switch voltage $u_{sw}(k+1)$ equals to the current used switch state $u_{sw}(k|k-1)$. The sum function represents adding all the data for a given array and the length function derives the total numbers of the data in this array. The value of $S_{avg}(k)$ is always smaller than 1.

Therefore, the average switching frequency f_{avg} of the inverter can be defined as

$$f_{avg}(k) = S_{avg}(k)\, f_s/6 \tag{3.9}$$

where $f_s/6$ represents the equivalent switching frequency of the inverter for the FCS-MPC, which is described in Chapter 4.

In equation (3.6), the voltage vectors are expressed in a switching state form. Thus a set of voltage vectors in dq coordinate system needs to be derived for further computation. Since the switching states are firmly related to the $\alpha\beta$ coordinate system, the first step is to transfer the switching states into the voltage vectors in the $\alpha\beta$ coordinate system $U_{\alpha\beta}(k+1)$. Then the voltage vectors in the dq coordinate system $U_{dq}(k+1)$ can be achieved by introducing the electrical angle θ_r with the help of (2.3) and (2.37).

$$\begin{aligned} U_{\alpha\beta}(k+1) &= \tfrac{2}{3}U_{dc}\begin{bmatrix} 1 & -\frac{1}{2} & -\frac{1}{2} \\ 0 & \frac{\sqrt{3}}{2} & -\frac{\sqrt{3}}{2} \end{bmatrix} U_{sw}(k+1) \\ U_{dq}(k+1) &= \begin{bmatrix} \cos(\theta_r(k)) & \sin(\theta_r(k)) \\ -\sin(\theta_r(k)) & \cos(\theta_r(k)) \end{bmatrix} U_{\alpha\beta}(k+1) \end{aligned} \tag{3.10}$$

3.3.2.2 Angle compensation

In (3.10), when transferring the voltage vectors into the dq coordinate system, a constant electrical angle $\theta_r(k)$ at time step k is used. To improve the accuracy of selecting the voltage vectors, the angle compensation method which takes the angle variations into consideration can be utilized for help[12].

Instead of the electrical angle θ_r, it is assumed that the electrical rotating speed ω_r is constant during each time interval. Thus the electrical angle θ_r varies as

$$\theta_r(t) = \omega_r(t_k)\,(t - t_k) + \theta_r(t_k), \quad t_k \le t < t_k + T_s \tag{3.11}$$

Therefore, the voltage vectors in the $\alpha\beta$ coordinate system rotate with a constant speed $\omega_r(k)$ during the time interval t_k to $t_k + T_s$. The mean value of the electrical angle θ_r of the varying voltage vectors will be derived, and the pre-selection of input voltage vectors at time step k+1 can be approximated as

$$\begin{aligned} \theta_r(k+1) &\approx \theta_r(k) + \tfrac{T_s}{2}\omega_r(k) \\ U_{dq}(k+1) &= \begin{bmatrix} \cos(\theta_r(k+1)) & \sin(\theta_r(k+1)) \\ -\sin(\theta_r(k+1)) & \cos(\theta_r(k+1)) \end{bmatrix} U_{\alpha\beta}(k+1) \end{aligned} \tag{3.12}$$

3.3.2.3 States prediction

With the help of the discretization equation of the PMSM (3.3) or (3.4), future state values (i.e., future values of i_d and i_q) can be predicted by applying the set of the pre-selected voltage vectors as input.

At time step k, the states prediction equations can be defined as

$$\begin{aligned} x(k+1|k) &= A_d(k)x(k|k) + B_d(k)u(k|k-1) + E_d(k) \\ x(k+2|k) &= A_d(k+1)x(k+1|k) + B_d(k+1)u(k+1|k) + E_d(k+1) \\ x(k+3|k) &= A_d(k+2)x(k+2|k) + B_d(k+2)u(k+2|k) + E_d(k+2) \\ &\cdots\cdots \end{aligned} \tag{3.13}$$

The explanation of how the states prediction works is listed below.

1. For the first equation, to predict the states $x(k+1|k)$ at the next time step k+1, the voltage vector $u(k|k-1)$ selected at the previous step k-1 is applied as input.

2. For the second equation, $u(k+1|k)$ has 4 possible values to generate the PMSM at the next time step k+1. By applying these 4 values to the second equation, 4 corresponding states $x(k+2|k)$ can be derived. A verification of how these four states operate is made based on the cost functions (in the next section) and the corresponding control decision vector that minimizes the cost function is chosen as optimal. This optimal voltage vector will be selected as an input at the next time step k+1. This briefly expresses how FCS-MPC works when the prediction horizon N=1.

3. If the prediction horizon N=2, the third equation needs to be included in. Since there are 4 possible voltage values of $u(k+1|k)$ and 4 possible corresponding states of $x(k+2|k)$ in the second equation, if a further prediction till the time step k+2 is made based on these 4 possible voltage values of $u(k+1|k)$, there exist 16 possible values for the voltage vector $u(k+2)$. In the same way, 16 corresponding states $x(k+3|k)$ at time step k+3 will be derived and the optimal case will be verified among them. Therefore, the selected voltage vector $u(k+1|k)$ at time step k+1 can be selected according to the 16 states of $x(k+3|k)$ at time step k+3.

4. More prediction equations are needed if a higher prediction horizon is required. This implementation method is similar as described in the previous step.

3.3.3 Cost function

The solution of a given equation $f(i_d, i_q) = 0$ gives the current states trajectory in $i_d - i_q$ plane (i.e., state plane). For the current vectors with $f(i_d, i_q) \neq 0$, functions like $|f(i_d, i_q)|$ or $|f(i_d, i_q)|^2$ help to define the error from the current states trajectory $f(i_d, i_q) = 0$.

In this thesis, the form of $|f(i_d, i_q)|^2$ is used for a better error sensitivity. The cost functions can be divided into the following three targets: torque tracking, attraction region and limitation.[8][9]

3.3.3.1 Torque tracking

In order to generate the electromagnetic torque as the reference required, a torque tracking cost function is formulated by penalizing the torque error. According to (2.13), the cost function can be expressed as

$$\begin{aligned} c_T &= (T_{em} - T_{ref})^2 \\ &= (\tfrac{3}{2} n_p(\psi_d i_q - \psi_q i_d) - T_{ref})^2 \end{aligned} \tag{3.14}$$

3.3.3.2 Attraction region

For low speed operation, Maximum Torque Per Ampere (MTPA) control strategy is selected as mentioned in Chapter 2, it helps to increase the operating efficiency by generating the maximum torque for the same current magnitude. Based on (2.22), the cost function to achieve MTPA can be written as

$$\begin{aligned} c_{A_1} &= A_1^2 \\ A_1 &= L_{qq} i_d^2 + L_{dd} i_q^2 - (L_{dq} + L_{qd}) i_d i_q - \psi_d i_d - \psi_q i_q \end{aligned} \tag{3.15}$$

As the speed increases, Field Weakening (FW) control strategy is applied to replace the MTPA control strategy when the back EMF exceeds voltage limit as shown in (2.29). The FW cost function compared with (3.15) is expressed as

$$\begin{aligned} c_{A_2} &= A_2^2 \\ A_2 &= (\tfrac{U_{dc}}{\sqrt{3}|\omega_r|} - \sqrt{\psi_d^2 + \psi_q^2}) I_r \end{aligned} \tag{3.16}$$

where $U_{dc}/\sqrt{3}$ represents the rated PMSM terminal voltage, and I_r is the rated PMSM current.

The unit unification of the cost functions (3.15) and (3.16) enables to make the error away from their trajectories comparable. The alternating criteria between these two attraction regions is defined as

$$c_A = \begin{cases} c_{A_1} & | \quad c_{A_1} \leq c_{A_2} \\ c_{A_2} & | \quad c_{A_2} \leq c_{A_1} \end{cases} \tag{3.17}$$

The alternating criteria (3.17) will be active with the help of voltage limit equation (3.20).

3.3.3.3 Limitation

Limitation cost functions are necessary to avoid the current states reaching undesired operation regions.

1. Current limit
The current amplitude of the PMSM should not exceed its maximum value (2.27).

This constraint can be imposed by adding the following penalty term in the limitation cost functions

$$\begin{aligned} c_{L_1} &= \begin{cases} {L_1}^2 & | \quad L_1 \leq 0 \\ 0 & | \quad L_1 \geq 0 \end{cases} \\ L_1 &= I_r - \sqrt{i_d^2 + i_q^2} \end{aligned} \tag{3.18}$$

2. Symmetric axis
Since the MTPA equation indicates two symmetric curves, so the following cost function helps to restrict the current states operating on the left side of the symmetric axis as calculated in (2.26).

$$\begin{aligned} c_{L_2} &= \begin{cases} {L_2}^2 & | \quad L_2 \leq 0 \\ 0 & | \quad L_2 \geq 0 \end{cases} \\ L_2 &= \frac{i_{d1}+i_{d2}}{2} - i_d \end{aligned} \tag{3.19}$$

3. Voltage limit
In addition to forcing the states to evolve on the Field Weakening trajectory (3.16), a cost function limiting the states within the shrinking ellipse is necessary to help alternating the control strategy from MTPA to FW (3.17).

$$\begin{aligned} c_{L_3} &= \begin{cases} {L_3}^2 & | \quad L_3 \leq 0 \\ 0 & | \quad L_3 \geq 0 \end{cases} \\ L_3 = A_2 &= \left(\frac{U_{dc}}{\sqrt{3}|\omega_r|} - \sqrt{\psi_d^2 + \psi_q^2}\right) I_r \end{aligned} \tag{3.20}$$

4. MTPV
In order to achieve a higher speed control of the PMSM, sacrificing the tracking of the reference torque is permitted. The MTPV trajectory equation (2.35) helps to improve the stability by restricting the states to its right side.

$$\begin{aligned} c_{L_4} &= \begin{cases} {L_4}^2 & | \quad L_4 \leq 0 \\ 0 & | \quad L_4 \geq 0 \end{cases} \\ L_4 &= \frac{\psi_d^2}{L_{qq}} + \frac{\psi_q^2}{L_{dd}} + \frac{L_{dq}+L_{qd}}{L_{dd}L_{qq}}\psi_d\psi_q - \left(1 - \frac{L_{dq}L_{qd}}{L_{dd}L_{qq}}\right)(\psi_d i_d + \psi_q i_q) \end{aligned} \tag{3.21}$$

5. Total cost function
The total cost function is the weighted sum of the three target costs over prediction horizon N, where cost weights q are tunable parameters for penalty.

$$Cost = \sum_{i=1}^{N} \left(q_T c_T(k+1+i) + q_A c_A(k+1+i) + q_L c_L(k+1+i)\right) \tag{3.22}$$

where

$$c_L(k+1+i) = c_{L_1}(k+1+i) + c_{L_2}(k+1+i) + c_{L_3}(k+1+i) + c_{L_4}(k+1+i) \tag{3.23}$$

A normalization of each cost function can be made so that each term remains in the same order of magnitude. It helps in selecting tuning weights more intuitively. A smaller value of q_T should be applied when the speed exceeds its maximum value for a given torque reference.

3.3.3.4 Decision of the switching state

For a high prediction horizon N, 4^N results are verified in the total cost function. The 'Modulo 4' operation can be introduced to help finding the corresponding switching state for the two-level VSI. No matter how long the prediction horizon N is used, the FCS-MPC applies only the first element ($U_{sw}(k+1|k)$) of the optimal control sequence. The arrangement of the cost function results is originated from the repeating sequence of the 4 voltage vectors in $U_{sw}(k+1)$ as shown in Figure 3.3. If it is given that the order of the cost function results is (1,2,3,4,5,6,7,8,...), the result after the operation of 'Modulo 4' is (1,2,3,0,1,2,3,0,...). Then, by replacing '0' with '4', the order is arranged in (1,2,3,4,1,2,3,4...). Therefore, the relation between the order of the cost function results and their corresponding switching states in $U_{sw}(k+1)$ becomes intuitive.

4

Case Setup

4.1 Electric drive system

A drive system including an adaptive PI-controller, SVPWM based control scheme and non-linear PMSM model is used as a benchmark for the MPC controller derived in this thesis. The general structure of this electric drive system is illustrated in Figure 4.1. Except for the Dyno system, this thesis deals with reframing all the other blocks based on the FCS-MPC algorithm.

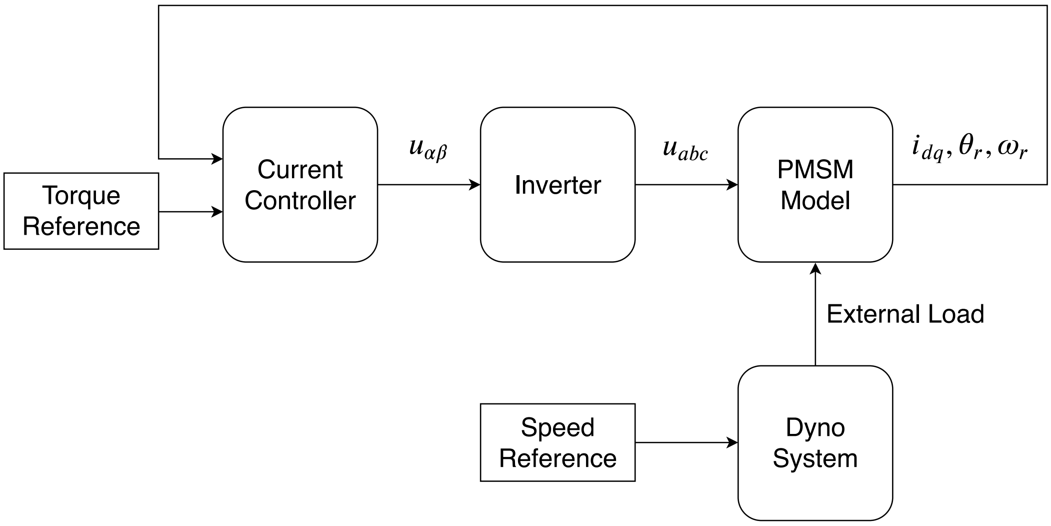

Figure 4.1: Structure of the electric drive system

For the benchmark system:

(1) The current controller first converts the torque reference into current references through the LUTs, the current references are adjusted if field weakening control strategy needs to be applied. For the speed tracking, the dyno system transfers the speed reference into a corresponding external torque to the PMSM model, so that the torque difference between the electromagnetic torque and the external torque can generate the required speed. Both torque reference and speed reference are step signals, and a rate limiter is connected to each of them. This enables the torque and

speed to increase in a smooth way so that the mechanical parts such as the rotor shaft and gearbox can be protected.

(2) The state space function of the PMSM model is formulated with flux based currents ($i_d(\psi_d, \psi_q)$,$i_q(\psi_d, \psi_q)$) where fluxes are the system states. The PI controller consists of the MTPA and the Field Weakening control strategies and its sampling frequency is 8 [kHz]. The inverter model can generate the three-phase voltages by using the SVPWM scheme to derive the averaged voltage vector during each sampling interval. The switching frequency of the inverter, including all three-phases, using SVPWM scheme is 8 [kHz] which is synchronized with the PI controller.

This thesis starts from formulating the continuous PMSM model using currents as the system states with the given parameters $\psi_d(i_d, i_q)$, $\psi_q(i_d, i_q)$ and R_s. As a result of this, discretization models can be made to realize the current predictions and controls. Finally, an FCS-MPC controller is designed with only 4 of the 8 inverter switching states as inputs to select the optimal voltage decision as described in Chapter 3.

4.2 System setup

4.2.1 Operation scenarios

Table 4.1 presents the two operation scenarios used in the simulation. A torque reference signal T_{ref} is initiated for the electric drive system, then the speed reference n_{ref} begins to increase gradually from 0 to 15000 [rpm]. Finally a negative signal $-T_{ref}$ is added to the torque reference giving $T_{ref} = 0$ when the speed maintains at 15000 [rpm]. Therefore, different operation conditions can be reached as discussed in Chapter 2. For steady-state analysis, the increasing speed reference n_{ref} is set to maintain for 0.01 [s] at the levels of 0, 2000, 4000, 6000, 8000, 15000 [rpm] which includes all the operation regions: MTPA, FW with $T_{em} = T_{ref}$, FW with $T_{em} < T_{ref}$ and MTPV.

Table 4.1: Two operation scenarios

	Scenario 1	Scenario 2
Torque reference T_{ref}	1 [pu]	0.5 [pu]
Torque rate limiter	25 [pu/s]	
Speed reference n_{ref}	15000 [rpm]	
Speed rate limiter	10000 [rpm/s]	

4.2.2 System parameters

Table 4.2-4.4 list the main parameters used in the electric drive system below. For confidentiality concern, most of the system parameters are expressed in the form of per unit value.

Table 4.2: PMSM parameters

PMSM type	IPM
Flux ψ_d, ψ_q	Figure 2.3
Partial inductances $L_{dd}, L_{dq}, L_{qd}, L_{qq}$	Figure 2.4
Stator Resistance R_s	1 [pu]
Pole pairs n_p	4

Table 4.3: Configuration of the FCS-MPC and two-level VSI

FCS-MPC controller	
Sampling frequency f_s	48, 96 [kHz]
Prediction horizon N	2, 5
Cost weights (q_T, q_A, q_L)	Table 4.4
Two-level VSI Model	
Switching frequency f_{sw}	$f_s/6$
DC Voltage U_{dc}	600 [V]
Rated current I_{rms}	0.6 [pu]

Table 4.4: FCS-MPC cost weights under different scenarios

Scenario	1	2
Cost weights 1 (q_T, q_A, q_L)	(2,1,30)	(2,1,30)
Speed range 2	5500-10000 [rpm]	5500-9000 [rpm]
Cost weights 2 (q_T, q_A, q_L)	(0.03,1,2)	(0.4,0.01,3)
Speed range 3	10000-15000 [rpm]	9000-15000 [rpm]
Cost weights 3 (q_T, q_A, q_L)	(0.03,0.02,5)	(0.1,0.01,5)

The tuning of the cost weights can be quite difficult and is highly correlated to the torque and speed levels. Unlike the two-level VSI operated under SVPWM scheme changes its switching states 6 times during one sampling interval, the two-level VSI used for the FCS-MPC only changes its switching states once at each sampling interval. Therefore, for the FCS-MPC control scheme, the equivalent switching frequency of the inverter is 1/6 of the FCS-MPC sampling frequency. In order to make the performance of switching losses comparable between the PI and FCS-MPC control schemes, the default configuration of the FCS-MPC is set to operate under f_s=48 [kHz] and N=2. Different configurations of sampling frequency and prediction horizon are used for comparison and analysis of the FCS-MPC features.

5

Result

5.1 Verification of the FCS-MPC model

5.1.1 Evaluation of the discretized models

In order to guarantee that the discretized models of the PMSM have enough accuracy to predict the states in the FCS-MPC, the simulation results of i_d, i_q under the Forward Euler method and Zero-Order Hold method are evaluated. Figure 5.1 and Figure 5.2 present the compared simulation results at two different sampling frequencies. The comparison includes the current time plots and the current error plots between the continuous and discretized models.

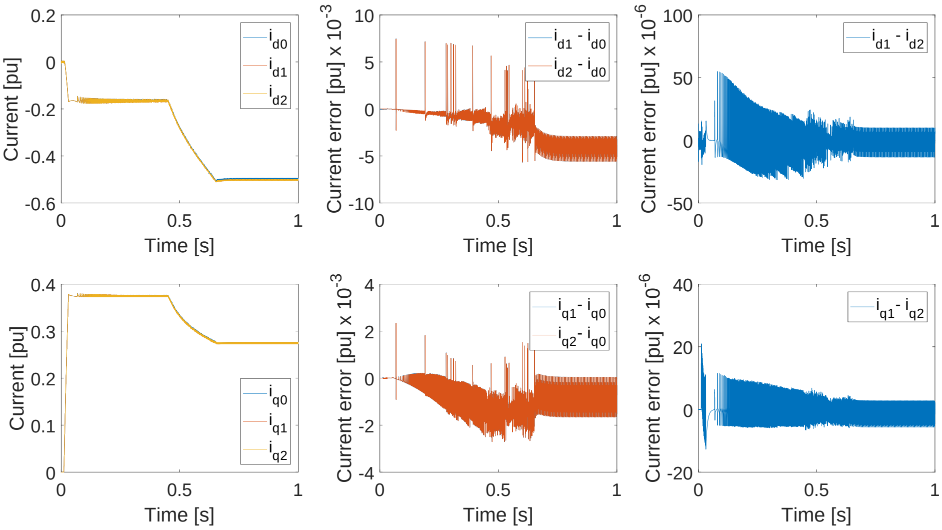

Figure 5.1: Evaluation of the discretized models (sampling frequency: 8 [kHz]), the subscripts of 0,1,2 represent the results are based on the continuous, Euler Forward and Zero-order Hold models

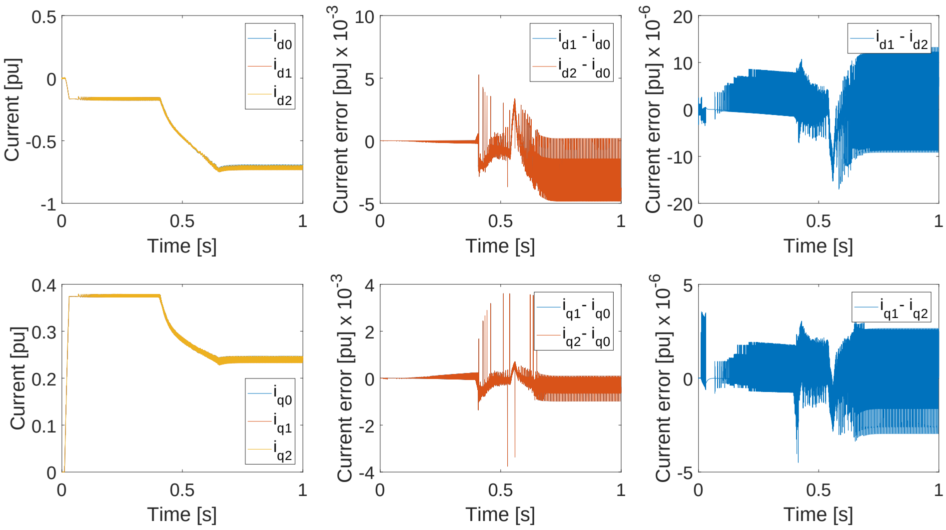

Figure 5.2: Evaluation of the discretized models (sampling frequency: 48 [kHz]), the subscripts of 0,1,2 represent the results are based on the continuous, Euler Forward and Zero-order Hold models

The two evaluations are performed with the following setup:

(1) Three PMSM models are utilized: the continuous model with currents as system states, two discretized models using Euler Forward and Zero-order Hold method based on the continuous model. The PI controller in the benchmark system helps to generate the voltage input for the three PMSM models. The sampling frequency of the PI controller cannot be set smaller than 6 [kHz] for high speed operation, so 8 [kHz] and 48 [kHz] are selected for the evaluations.

(2) At 0.01 [s], a torque reference 0.5[pu] is applied and reaches its value at 0.05 [s], at the same time the speed reference 6000 [rpm] is excited and the value is achieved at 0.65 [s].

(3) For each figure, the first row presents the simulation results of i_d, while the second is related to i_q. The first column of the figure illustrates the current time plots under the three PMSM models. The second column shows the current errors of each discretized model with the continuous model. The third column compares the current errors between the two discretized models.

In general, the current time plots of the discretized model have no obvious errors between each models. For the second column plots, the magnitude of current errors between the discretized and continuous model is 10^3 times smaller than the current values. It can be found that these current errors keep increasing as the speed goes up. Since the term $E_d(k)$ in the discretized model (3.3) or (3.4) is proportional to the electrical angle speed ω_r, the error of the term $E_d(k)$ increases as the speed goes up.

Furthermore, for the third column plots, the magnitude of the current errors between the two discretized models is 10^6 times smaller than the current values. This means that the performance of two discretized models is quite close. As the sampling frequency f_s increases from 8 [kHz] to 48 [kHz], these current errors have been reduced since the accuracy of Euler Forward is largely improved at high sampling frequency.

5.1.2 Current ripple analysis

At steady-state, since only 8 switching states of the two-level VSI help generate the input voltage vectors, the currents fluctuate in a repeating pattern to maintain the desired values. As a result of this, current ripple exists and is highly correlated with the one step difference $\Delta x = x(k+1) - x(k)$. The discretized model based on Euler Forward method (3.3) is used to approximate the one step difference. The one step difference can be formulated by

$$\Delta x(k) = J^{-1}(Ax + Bu + E)T_s \tag{5.1}$$

Present it in complete form

$$\begin{bmatrix} \Delta i_d \\ \Delta i_q \end{bmatrix} = \begin{bmatrix} \frac{\partial \psi_d}{\partial i_d} & \frac{\partial \psi_d}{\partial i_q} \\ \frac{\partial \psi_q}{\partial i_d} & \frac{\partial \psi_q}{\partial i_q} \end{bmatrix}^{-1} \left(\begin{bmatrix} -R_s & 0 \\ 0 & -R_s \end{bmatrix} \begin{bmatrix} i_d \\ i_q \end{bmatrix} + \begin{bmatrix} u_d \\ u_q \end{bmatrix} + \begin{bmatrix} \omega_r \psi_q \\ -\omega_r \psi_d \end{bmatrix} \right) T_s \tag{5.2}$$

For the PMSM used in this thesis, the stator resistance R_s is relatively small, the value $R_s i$ can be neglected when compared to the input voltage and the back EMF items. For the fluxes ψ_d, ψ_q and their partial inductances (2.10), it is assumed that the variations of these values differences are ignorable. Thus, it can be summed that the current ripples (one step difference) are mostly affected by the sampling frequency, voltage level and rotational speed.

In this thesis, the low partial inductances of the PMSM are very low and a high DC-link voltage is used for the inverter. Thus the simulation result operated at 8 [kHz] has quite big current ripples so that the current states trajectory cannot be detected on the current states figure and it is hard to evaluate the performance of trajectory tracking (MTPA and FW). Therefore, the FCS-MPC sampling frequencies compared in this thesis are 48 and 96 [kHz].

5.1.3 Improvement of the cost function

Figure 5.3 and Figure 5.4 demonstrate the simulation results based on the cost functions which are discussed in Chapter 3. The main setup parameters are listed in Table 5.1.

Table 5.1: Setup parameters

Torque reference T_{ref}	1 [pu] (solid cyan curve)
Speed reference n_{ref}	5200 [rpm]
Cost weights (q_T, q_A, q_L)	(2,1,30)
Sampling frequency f_s	48, 96 [kHz]
Prediction horizon N	2
Simulation time t	0.6 [s]

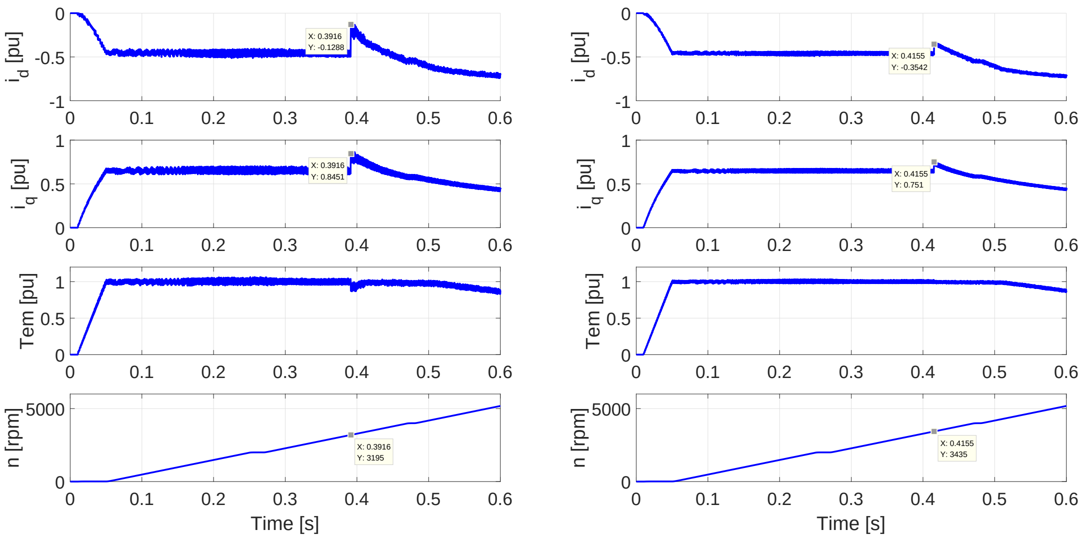

(a) $f_s = 48$ [kHz] **(b)** $f_s = 96$ [kHz]

Figure 5.3: Time plots before improvement

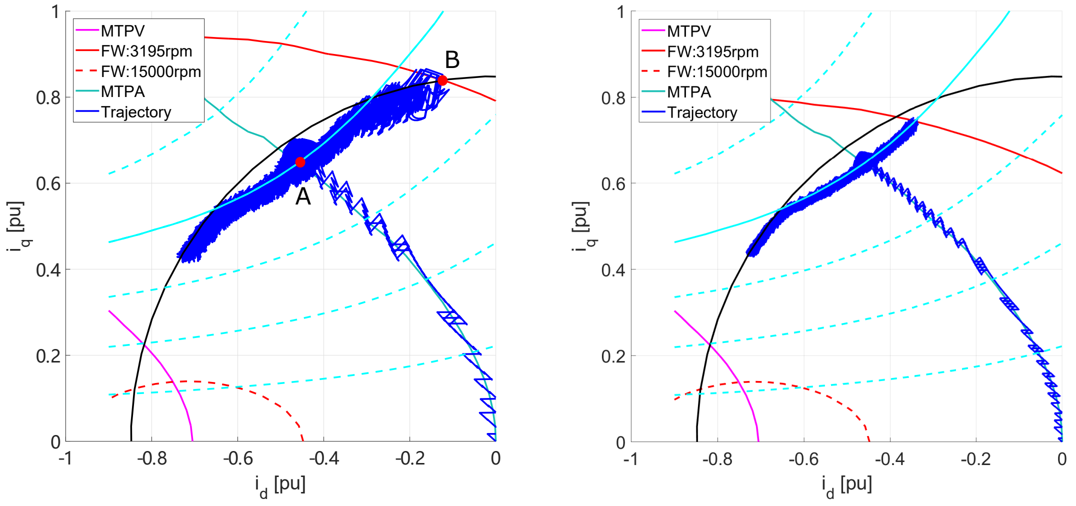

(a) $f_s = 48$ [kHz] **(b)** $f_s = 96$ [kHz]

Figure 5.4: Current states trajectory before improvement

The simulation is carried out to realize the automatic control strategy transformation from MTPA to FW based on the FCS-MPC control scheme. For the simulation result under the default sampling frequency of 48 [kHz], it can be observed that the current states move into the wrong direction (when the speed is 3195 [rpm]) just before the shrinking FW ellipse arrives the intersection point A between the MTPA and 1 [pu] torque curve. The current states meet the 3195 [rpm] FW ellipse at point B and evolve along the 1 [pu] torque curve as the FW ellipse shrinks. Therefore, an error performance of premature tracking exists and cannot be fixed by tuning the cost weights. The same problem occurs for a higher sampling frequency case (96 [kHz]) and the error occurs when the speed is 3435 [rpm].

One common phenomenon for the two different f_s cases is that the current keeps following the reference torque curve during the error operation sections, this proves that the torque tracking cost function (3.14) works properly. In order to analyze how the cost functions of attraction region (3.15)-(3.17) and limitation (3.18)-(3.21) work during the error operation sections, the cost function values along the 1 [pu] T_{ref} curve are evaluated as shown in Figure 5.5 and Figure 5.6.

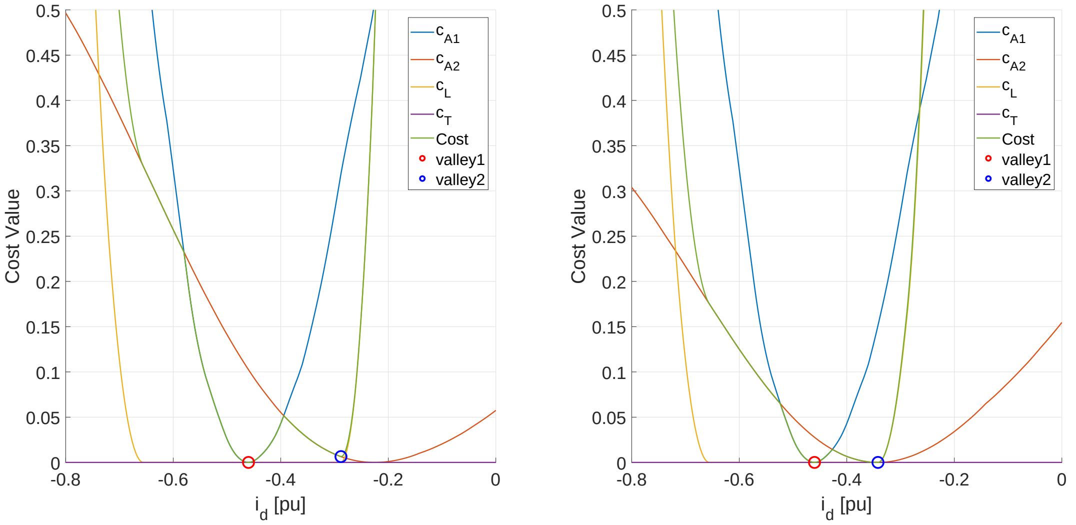

(a) Costs along the 1 [pu] torque curve when the rotational speed is 3195 [rpm]

(b) Costs along the 1 [pu] torque curve when the rotational speed is 3435 [rpm]

Figure 5.5: Cost analysis along the T_{ref} =1 [pu] curve

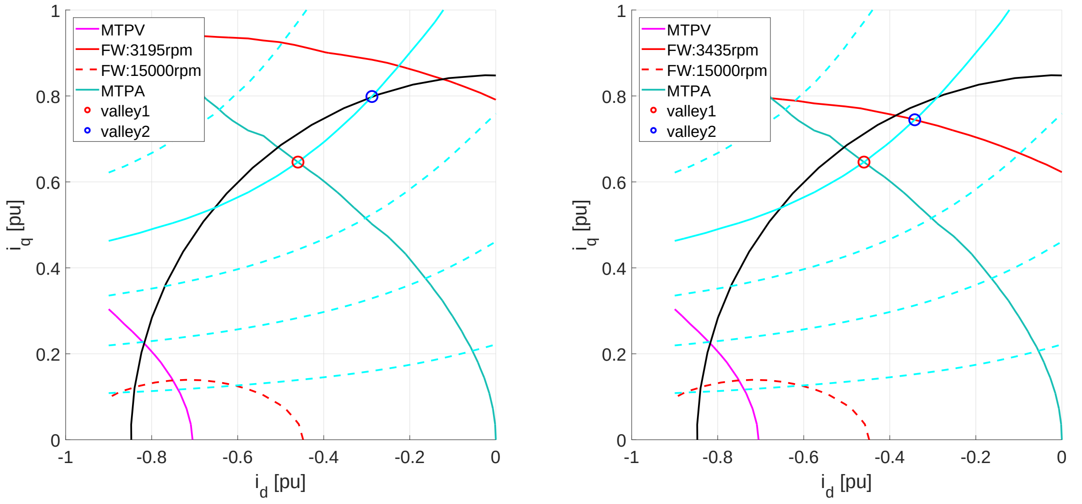

(a) Two valley points when rotational speed is 3195 [rpm]

(b) Two valley points when rotational speed is 3435 [rpm]

Figure 5.6: Two valley points along the T_{ref} =1 [pu] curve

From Figure 5.5, it can be seen that the total cost (green) is a 'W' shape plot along the 1 [pu] torque curve when the rotational speed is higher than 3000 [rpm]. This 'W' shape plot is mainly composed by the steady 'V' shape c_{A_1} and the 'V' shape c_{A_2} which keeps 'left-moving' as the speed goes up. This leads to the problem that there always exist two valley points during the approach of the two 'V' shape cost function parts. Since only 4 future switching states are evaluated in FCS-MPC, both valley points have the chance to be selected as the optimal decision of the FCS-MPC. Therefore, it is hard to guarantee that the current states can track the correct valley point, which explains why the error tracking performance cannot be fixed by tuning the cost weights.

Therefore, improvement should be made for the cost functions to avoid the 'W' shape of total cost. Since the operation points under FW and MTPV are constantly located on the left side of the MTPA trajectory, an enhanced symmetric axis limit trajectory (2.26) can be derived, which is a similar MTPA trajectory in parallel to the right side of the MTPA trajectory ($A_1(i_d, i_q) + 5 = 0$, where 5 represents a small bias to the MTPA trajectory). This can be done by reformulating (3.19) with the help of (3.15).

$$\begin{aligned} c^*_{L_2} &= \begin{cases} L_2^{*2} & | \quad L_2^* \leq 0 \\ 0 & | \quad L_2^* \geq 0 \end{cases} \\ L_2^* &= A_1 + 5 \\ &= L_{qq} i_d^2 + L_{dd} i_q^2 - (L_{dq} + L_{qd}) i_d i_q - \psi_d i_d - \psi_q i_q + 5 \end{aligned} \tag{5.3}$$

Figure 5.7 compares the difference between the origin (3.19) and enhanced (5.3) symmetric axis trajectories. Figure 5.8 presents the cost function values along the 1 [pu] T_{ref} curve after the improvement.

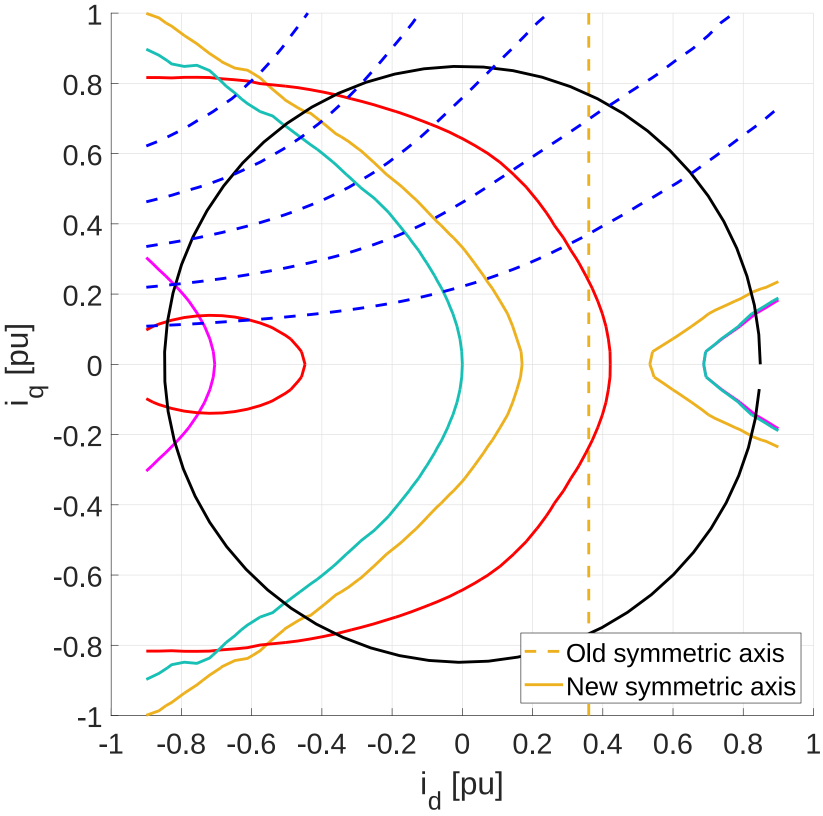

Figure 5.7: Improved symmetric axis trajectory

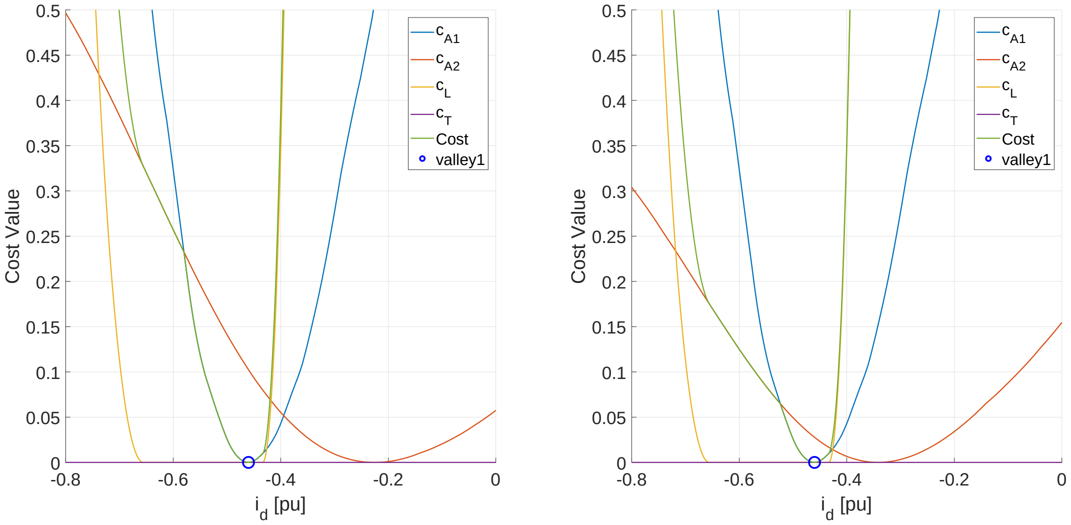

(a) Costs along the 1 [pu] torque curve when the rotational speed is 3195 [rpm]

(b) Costs along the 1 [pu] torque curve when the rotational speed is 3435 [rpm]

Figure 5.8: Cost analysis along the T_{ref} =1 [pu] curve after improvement

It can be found that the 'W' shape total cost situation has been removed in Figure 5.8. By executing the same simulations based on the improved cost functions, the simulation results are illustrated in Figure 5.9.

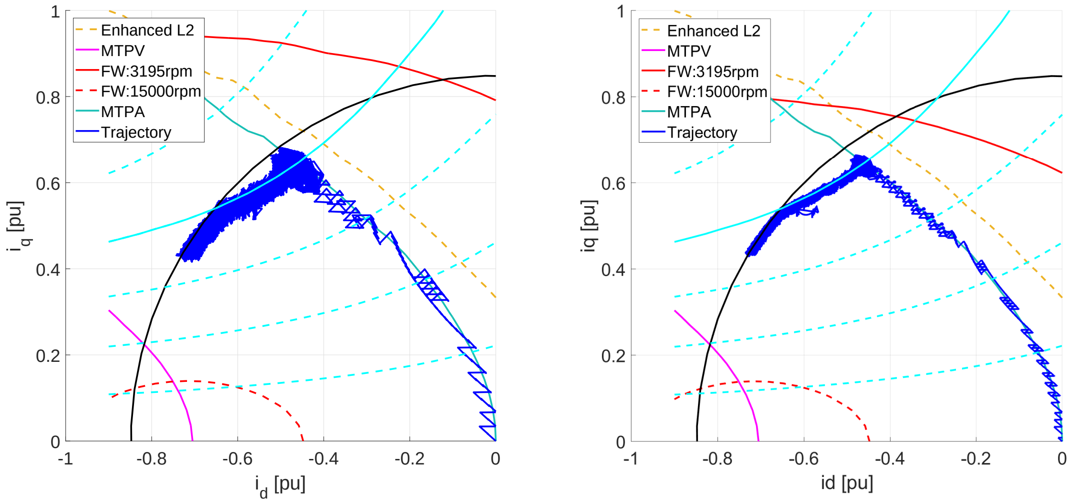

(a) $f_s = 48$ [kHz]

(b) $f_s = 96$ [kHz]

Figure 5.9: Current states trajectory after improvement

Compared to Figure 5.4, the error performance of premature tracking has been solved by introducing the enhanced symmetric axis limit cost function (5.3). The FCS-MPC model with the improved cost functions is applied for the following simulation cases.

5.2 Comparisons between the FCS-MPC and PI control schemes

This section focuses on the comparisons of the operation performances between the FCS-MPC and PI control schemes. In order to compare the ripple and switching performances, the inverter switching frequency under both control schemes is set to 8 [kHz]. Therefore, the PI controller is operated under the sampling frequency of 8 [kHz] while the FCS-MPC controller is operated under the sampling frequency of 48 [kHz]. The default prediction horizon N set for the FCS-MPC is 2.

5.2.1 Step response comparison

A step response is a convenient way to analyze the system features such as dynamic performance and its stability. In order to generate the step signal of T_{ref}, the torque rate limiter is disconnected. Figure 5.10 compares the step response performance between two different scenarios as shown in Table 4.1 (T_{ref} is 1 [pu] and 0.5 [pu]). The setup parameters of prediction horizon N and cost weights (q_T, q_A, q_L) used in the FCS-MPC controller are identical to those presented in Table 5.1. Quantities like overshoot and rise time are evaluated for torque tracking performance based on the simulation results.

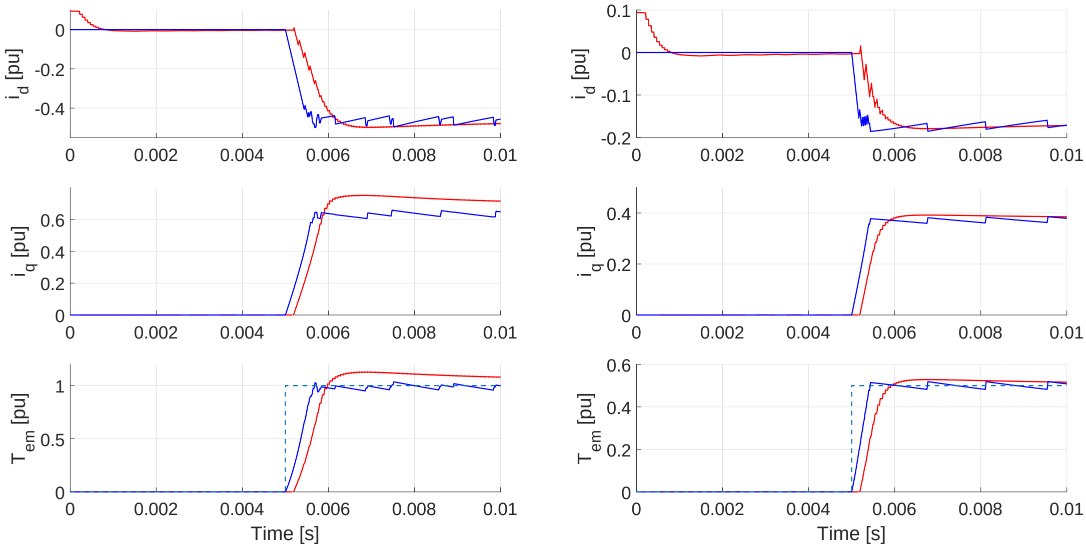

(a) Scenario 1 **(b)** Scenario 2

Figure 5.10: Step response comparisons (blue:FCS-MPC, red:PI)

The simulation results under the two different torque reference scenarios are quite similar. When the torque reference step signal is applied at 0.005 [s], the i_d, i_q, T_{em} in the PI cases begin to increase (decrease for i_d) gradually to their desired values after a short delay. The overshoot can be explicit found for the $T_{ref} = 1$ [pu] scenario.

Differently from the PI cases, the i_d, i_q, T_{em} values in the FCS-MPC cases increase (decrease for i_d) linearly to their desired values as soon as the torque reference step signal is applied and the rise and fall times are faster than for the PI cases. There is no overshoot for the FCS-MPC cases. However, at steady-state, i_d, i_q, T_{em} stay at the desired values with fluctuating ripples while the ripples in the PI cases are quite small.

In order to analyze the frequency performance of T_{em}, Gaussian response system $|H(\omega)| = e^{-\left(\omega^2/\sigma^2\right)}$ is introduced to approximate the bandwidth BW for the non-linear PMSM system[19]. The 10% to 90% rise time t_r of the system is needed to calculate the bandwidth which is defined as

$$BW \approx \frac{0.34}{t_r} \tag{5.4}$$

Table 5.2 lists the step response quantities of T_{em} as derived from the simulation results.

Table 5.2: Step response results

Cases	Overshoot [%]	rise time t_r [ms]	Bandwidth BW [Hz]
FCS-MPC at 1 [pu]	No	0.49	700
PI at 1 [pu]	12.9	0.57	600
FCS-MPC at 0.5 [pu]	No	0.33	1020
PI at 0.5 [pu]	5.9	0.48	710

According to the Nyquist-Shannon sampling theorem, the sampling frequency should be larger than twice of the bandwidth. The default sampling frequency used in this thesis is 48 [kHz], which is pretty larger than the twice of the system bandwidth.

5.2.2 Control performances comparison

In order to evaluate the control performances under different operation conditions which are mentioned in Chapter 2. Two scenarios (T_{ref}=1, 0.5 [pu]) are set to compare the different performances based on the FCS-MPC and PI. The PI controller functions properly for the two scenarios without any modification of the controller setup. However, for the FCS-MPC controller, its setups are different for the two scenarios as listed in Table 4.4.

To realize the proper FCS-MPC control for the whole operation conditions, it is concluded that the set of the cost weights (q_T, q_A, q_L) must be modified during the operations. Different from the PI control method, it is not intuitive to find the relations between the cost weights and their corresponding operation points[20][21]. Therefore, manual tuning of the cost weights is needed for the constantly varying operation scenarios.

5.2.2.1 Current states trajectory comparison

Figure 5.11 shows the current states trajectories based on FCS-MPC control and PI control when the reference torque is 1 [pu]. In general, both current states track the desired trajectories properly.

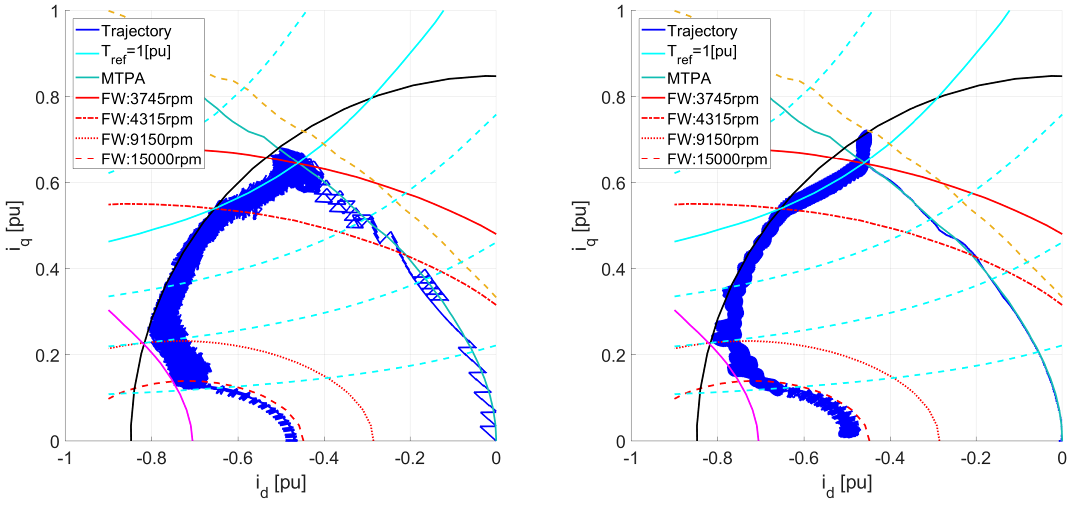

(a) FCS-MPC **(b)** PI

Figure 5.11: Comparison of current states trajectories based on scenario 1

When the rotational speed is below 3745 [rpm], the PMSM is operated under the MTPA control strategy. It is obvious that current states based on PI control scheme have a better tracking performance with smaller fluctuations around the MTPA trajectory when compared to the current states based on the FCS-MPC.

When the rotational speed exceeds 3745 [rpm], the FW control strategy is applied instead of the MTPA. At this point, the current states based on the PI control scheme encounter an error in the tracking performance while the FCS-MPC control scheme has solved similar problem in the previous section. Between 3745 [rpm] and 4315 [rpm], the 1 [pu] reference torque can be still achieved.

Beyond 4315 [rpm], the cost weights are tuned in order to increase the speed range by sacrificing the reference torque tracking. As the rotational speed reaches 9150 [rpm], the MTPV trajectory begins to take effect and it helps to maximize the generated torque. The tracking performances along the MTPV trajectory for both control schemes are not very good. The current states stop tracking the current limit circle before the rotational speed reaches 9150 [rpm] and begin to evolve along the right side of the MTPV trajectory.

A negative torque reference signal $-T_{ref}$ is added after the rotational speed reaches 15000 [rpm], the current states decrease along the 15000 [rpm] FW trajectory. It can be found that the current states trajectory based on the FCS-MPC control scheme has a more obvious tracking bias along the 15000 [rpm] FW trajectory.

The tracking errors at high speed along the MTPV and FW trajectories are discussed in the following section.

Similar to Figure 5.11, Figure 5.12 demonstrates the current states based on FCS-

MPC control and PI control when the reference torque is 0.5 [pu]. In general, both current states track the desired trajectories properly.

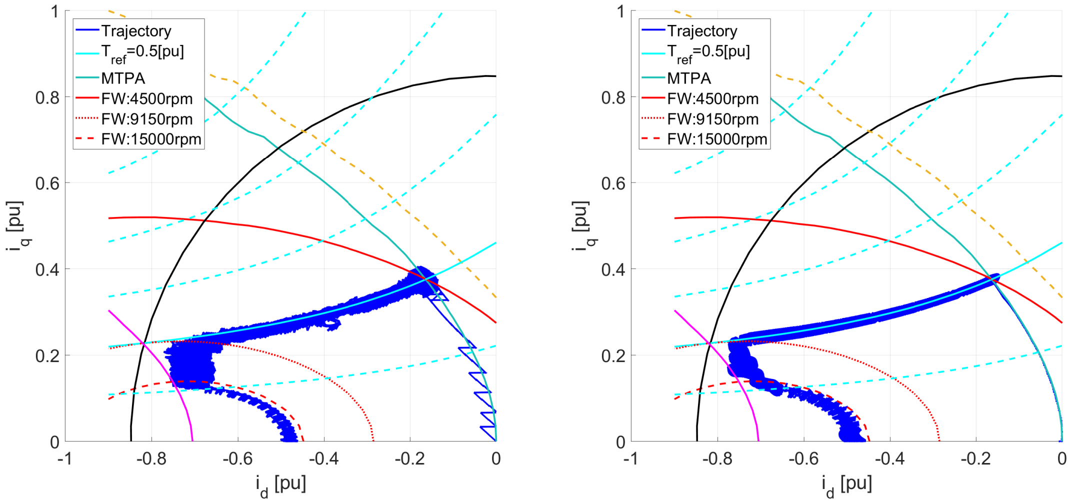

(a) FCS-MPC

(b) PI

Figure 5.12: Comparison of current states trajectories based on scenario 2

To avoid repetition, only differences of the tracking performance between T_{ref}=0.5 [pu] and T_{ref}=1 [pu] are discussed below.

For a lower torque reference 0.5 [pu], the MTPA control strategy is switched to the FW when a higher rotational speed 4500 [rpm] is reached. The error in the tracking performance for the PI control scheme is not explicit during the control strategy transformation between the MTPA and FW. When the rotational speed reaches the maximum speed 9150 [rpm] for the given torque reference 0.5 [pu], the MTPV is applied directly to help generate the optimal torque.

The detailed current and current ripple comparisons are mentioned in the following sections.

5.2.2.2 Time plot comparison

The simulation results of the two different scenarios (T_{ref}=1, 0.5 [pu]) are shown in Figure 5.13. It is quite clear that the time plots of $i_d, i_q, T_{em}, f_{avg}$ are not exactly the same.

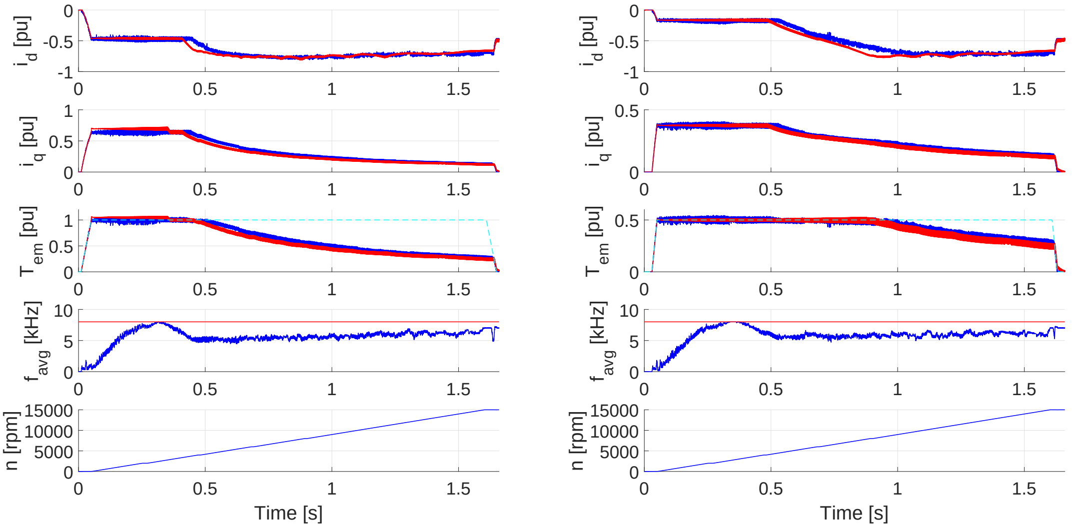

(a) Scenario 1 **(b)** Scenario 2

Figure 5.13: Comparison of time plots for two scenarios (blue:FCS-MPC, red:PI)

For the T_{ref}=1 [pu] scenario, the performance differences between the FCS-MPC and PI control schemes are listed as below.

(1) At the MTPA operation region, the generated torque T_{em} in the PI controller exceeds the 1 [pu] reference toruqe due to the error tracking of i_q. As the speed increases, i_q and T_{em} are decreased to track the reference torque properly (around 0.35 [s]). When the PMSM is required to lower its generated torque for high speed operation (around 0.5 [s]), the PI controller generates a slightly lower torque when compared to the FCS-MPC controller.

(2) The switching losses can be quantified by the defined average switching frequency f_{avg} (3.9). For the PI control scheme, since SVPWM is utilized for the inverter, the inverter always changes its switching states 6 times during one sampling interval. Therefore, the simulation result of the average switching frequency f_{avg} based on PI control stays at 8 [kHz] during the entire simulation cycle. However, f_{avg} based on the FCS-MPC control scheme keeps varying during the whole simulation intervals. During the rise of the torque reference, f_{avg} fluctuates around a low frequency of 1 [kHz]. When the torque reference is reached, f_{avg} increases as the speed goes up and reaches the peak of 8 [kHz] at 0.3 [s] (The speed is 2500 [rpm] at this time). By then, f_{avg} begins to drop to about 5 [kHz] at 0.45 [s] and FW control strategy is active at the same time. This can be interpreted that, the FCS-MPC prefers to select more zero voltage vectors during the start up and select more full length voltage vectors at the 'rated' operation point (around 0.45 [s]). As a result of this, the FCS-MPC owns the same trend to select the zero or full length voltage vectors when in the middle interval, this explains why the peak f_{avg} occurs when the speed is 2500 [rpm]. For the rest of the operation intervals, f_{avg} increases slowly to reach the 7 [kHz]. Therefore, it can be summed that the switching losses of the FCS-MPC

control scheme are always lower than that of the PI control scheme.

The simulation results based on the T_{ref}=0.5 [pu] scenario share the same performance with the T_{ref}=1 [pu] scenario. Thus the comparisons between the FCS-MPC and PI control schemes are omitted.

5.2.2.3 Ripple comparison

To analyze the currents and torque ripple at steady-state, the speed reference n_{ref} is set to increase in steps from 0 to 15000 [rpm], each speed is kept for 0.01 [s] at the levels of 0, 2000, 4000, 6000, 8000, 15000 [rpm] in order to reach steady-state. Figure 5.14 illustrates the steady-state currents and torque time plots which are intercepted from Figure 5.13. Each 0.01 [s] time interval in Figure 5.14 (0-0.01 [s], 0.01-0.02 [s], 0.02-0.03 [s], etc.) represents the steady-state time plots at the speed level of 0 [rpm], 2000 [rpm], 4000 [rpm] and so on.

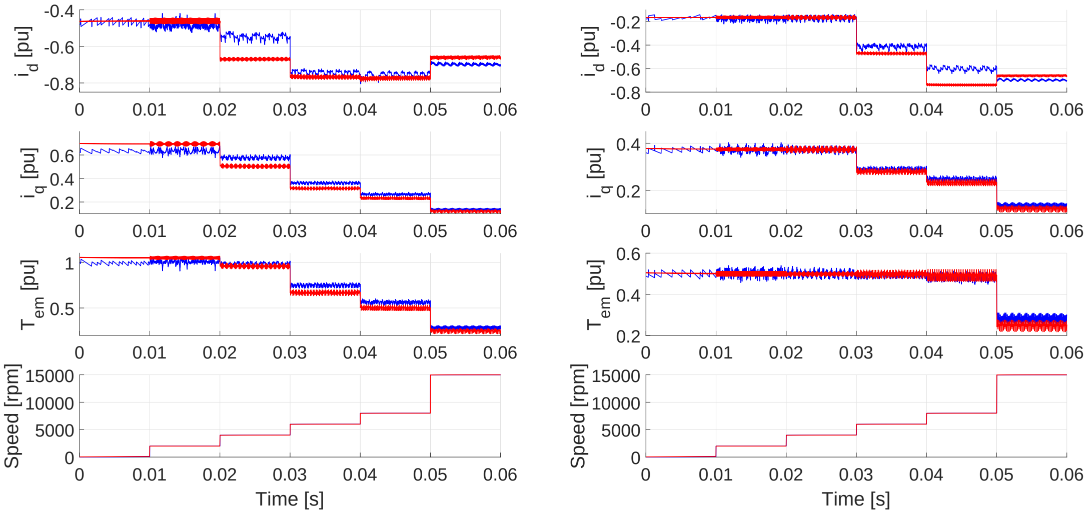

(a) Scenario 1 **(b)** Scenario 2

Figure 5.14: Steady state time plots (blue:FCS-MPC, red:PI)

In general, the steady-state currents and torque based on the PI control scheme are of sinusoidal shape and have smaller peak to peak ripple when compared to those based on the FCS-MPC control scheme. Two bar plots of the peak to peak ripple at different speed levels are presented in Figure 5.15. This enables a clear comparison of the ripple performances between the two control schemes.

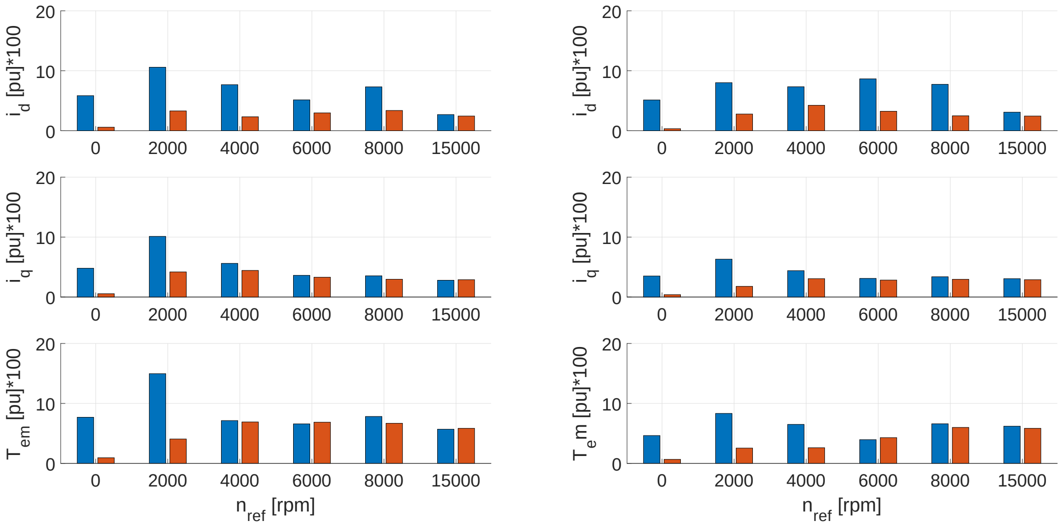

(a) Scenario 1 **(b)** Scenario 2

Figure 5.15: Comparison of ripples for two scenarios (blue:FCS-MPC, red:PI)

The ripple performances can be concluded as follows.

(1) At 0 speed, the current ripples of i_d, i_q and the torque ripple of T_{em} under PI are relatively small. 2000 [rpm] is a speed point which brings the huge ripple performances to this FCS-MPC scheme. It can be inferred that, at low speed, the voltage vector length needed is below $U_{dc}/\sqrt{3}$. And since FCS-MPC can only use the full vector length, the ripple will be high. For higher speed operation, where larger voltage vector length is needed, thus the ripple is lower.

(2) The current ripple of i_d, with FCS-MPC, is always more than twice as high compared to the ripple when using the PI control scheme, for speeds below 8000 [rpm]. When the speed is 15000 [rpm], the current ripple of i_d between the two control schemes are close.

(3) For the current ripple of i_q and the torque ripple of T_{em}, the ripple between the two control schemes are usually close except for when the speed is 2000 [rpm].

5.3 Comparisons of the FCS-MPC control schemes based on different configurations

This section aims to explore how the performance of the FCS-MPC is affected by the different configurations that is listed in Table 4.3. The comparisons of the simulation results based on different sampling frequencies f_s and prediction horizons N are conducted in two different scenarios (T_{ref}=1, 0.5 [pu]).

In order to avoid the influence of the cost weights on the simulation results, the cost weights setup (Table 4.4) needs to be kept the same for the different FCS-MPC configurations. However, better simulation performance can be derived if the cost weights setup is tuned for a specific configuration. This explains that the cost weights of the FCS-MPC control scheme are very sensitive to the PMSM operation points (different torque and speed levels) as well as the controller configurations (different sampling frequencies and prediction horizons).

5.3.1 Comparison between different sampling frequencies

5.3.1.1 Current states trajectory comparison

Figure 5.16 and Figure 5.17 present the simulation results of the current states under two given scenarios (T_{ref}=1, 0.5 [pu]), both of each figure present two plots of the current states trajectory based on the FCS-MPC control scheme with two different sampling frequencies (48 [kHz] and 96 [kHz]).

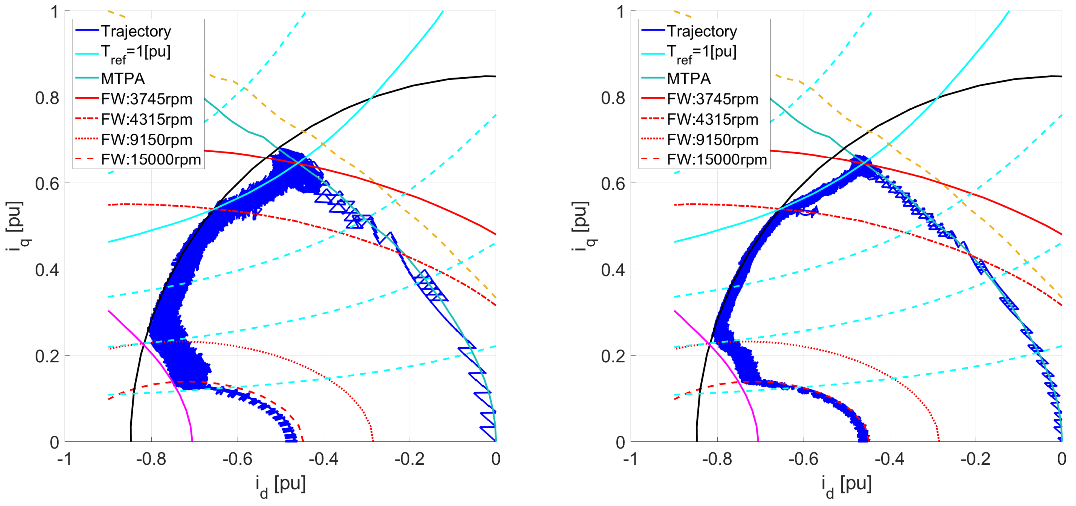

(a) f_s=48 [kHz], N=2

(b) f_s=96 [kHz], N=2

Figure 5.16: Comparison of current states trajectories based on scenario 1

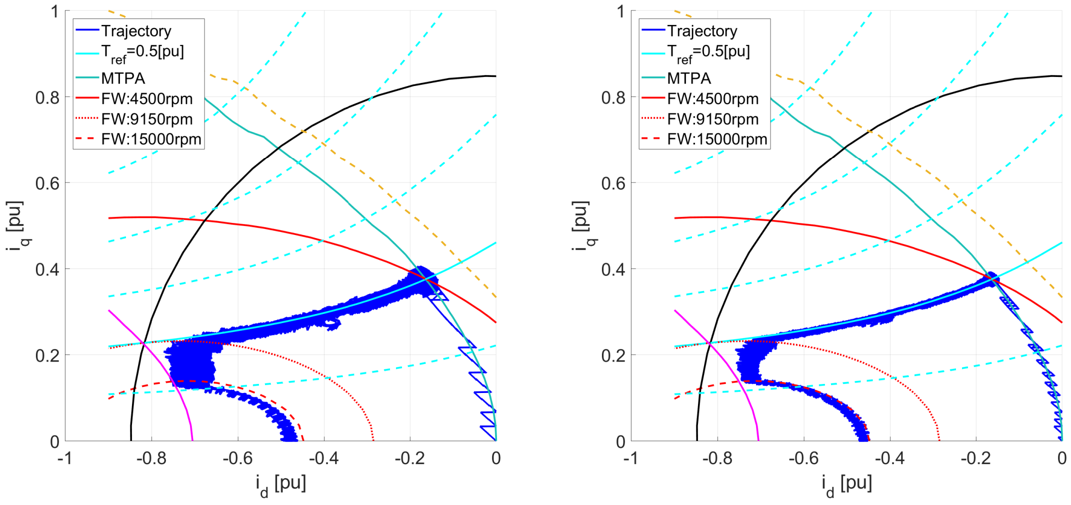

(a) f_s=48 [kHz], N=2 **(b)** f_s=96 [kHz], N=2

Figure 5.17: Comparison of current states trajectories based on scenario 2

After the higher sampling frequency 96 [kHz] is applied to the FCS-MPC, one explicit improvement for the tracking performance can be found. When a negative torque reference signal $-T_{ref}$ is added after the rotational speed reaches 15000 [rpm], the tracking bias problem along the 15000 [rpm] FW trajectory has been solved. It can be inferred that the tracking error along the FW trajectory at very high speed is due to the prediction error of the current states. Since the term $E_d(k)$ in the discretized model (3.3) or (3.4) is proportional to the electrical angle speed ω_r and sampling time T_s, the error of the term $E_d(k)$ increases as the speed goes up. As a result of this, a higher sampling frequency f_s helps to reduce the error of the current states.

5.3.1.2 Time plot comparison

The comparisons of the simulation results based on two different sampling frequencies are shown in Figure 5.18.

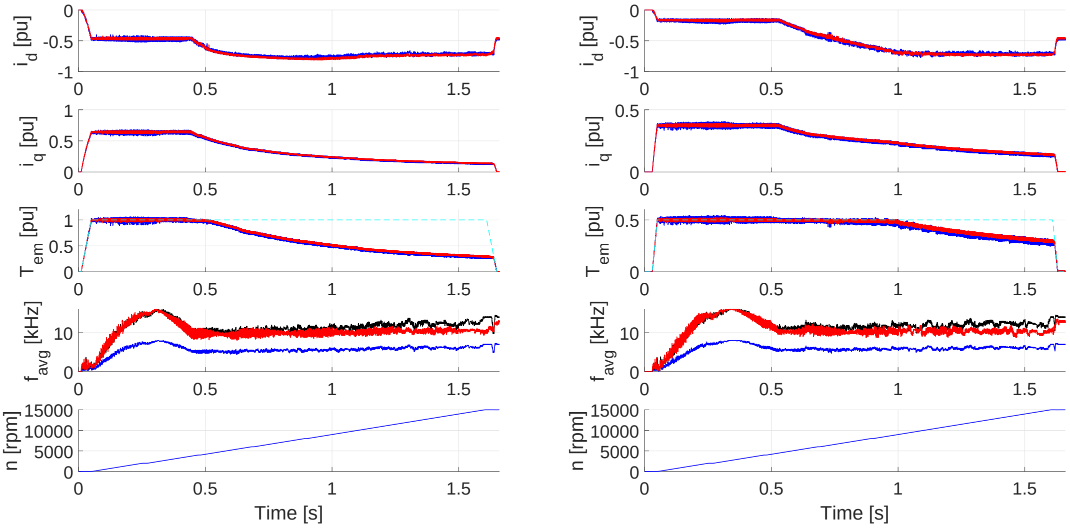

(a) Scenario 1 **(b)** Scenario 2

Figure 5.18: Comparison of time plots for two scenarios (blue:48 [kHz], red:96 [kHz])

The time plots of i_d, i_q, T_{em} under two different f_s are similar while the ripple of the 96 [kHz] configuration are smaller than that of the 48 [kHz] case. For the time plot of f_{avg}, the black curve is twice of the f_{avg} under 48 [kHz], this enables to compare the difference between the 48 [kHz] and 96 [kHz] cases. The f_{avg} under 96 [kHz] is exactly twice of the f_{avg} under 48 [kHz] during the generated torque can hold at the required T_{ref} (before 0.5 [s]). After that, the f_{avg} operated under 96 [kHz] always owns a lower frequency when compared to twice of the 48 [kHz] case. This means that a higher sampling frequency leads to a lower switching states change percentage. However, the switching losses are associated with the average switching frequency f_{avg}, thus the switching losses based on 96 [kHz] configuration is lower than twice of the switching losses of the 48 [kHz] case during FW operation region with $T_{em} < T_{ref}$.

5.3.1.3 Ripple comparison

Figure 5.19 illustrates the steady-state currents and torque time plots which are intercepted from Figure 5.18. Each 0.01 [s] time interval in Figure 5.14 (0-0.01 [s], 0.01-0.02 [s], 0.02-0.03 [s], etc.) represents the steady-state time plots at the speed level of 0 [rpm], 2000 [rpm], 4000 [rpm] and so on.

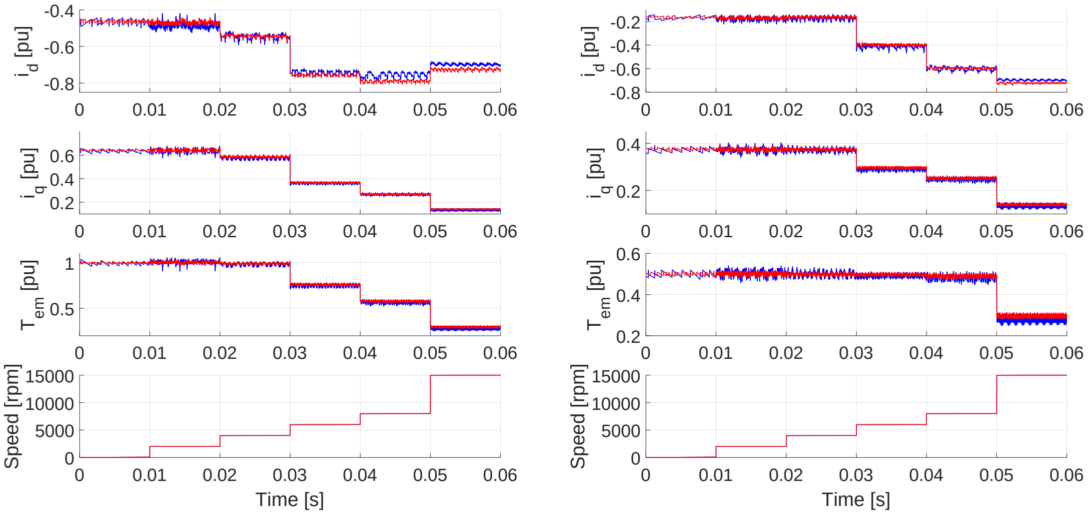

(a) Scenario 1 **(b)** Scenario 2

Figure 5.19: Steady state time plots (blue:48 [kHz], red:96 [kHz])

In general, the steady-state currents and torque based on higher switching frequency 96 [kHz] have smaller peak to peak ripple when compared to the default 48 [kHz] case. Two bar plots of the peak to peak ripple at different speed levels are presented in Figure 5.20.

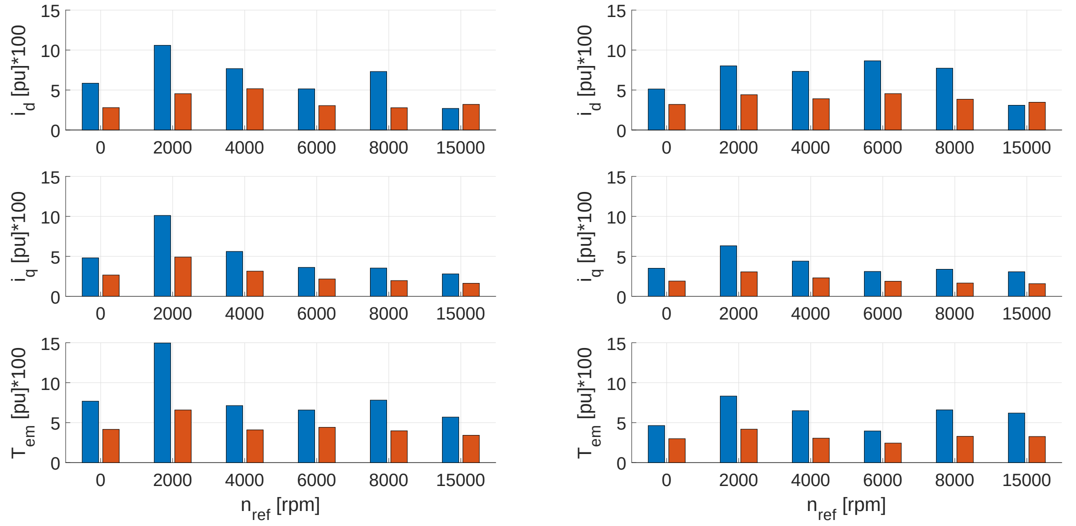

(a) Scenario 1 **(b)** Scenario 2

Figure 5.20: Comparison of ripples for two scenarios (blue:48 [kHz], red:96 [kHz])

It can be concluded that for most of the results presented in Figure 5.20, the currents and torque ripple for 96 [kHz] are nearly half of the corresponding ripple for the 48 [kHz] case. The reason for this is that the current ripple is approximately proportional to the sampling time T_s, which is shown in (5.2).

5.3.2 Comparison between different prediction horizons

5.3.2.1 Current states trajectory comparison

Figure 5.21 and Figure 5.22 present the simulation results of the current states under two given scenarios (T_{ref}=1, 0.5 [pu]), both of each figure present two plots of the current states trajectory based on the FCS-MPC control scheme with two different prediction horizons (N equals to 2 and 5).

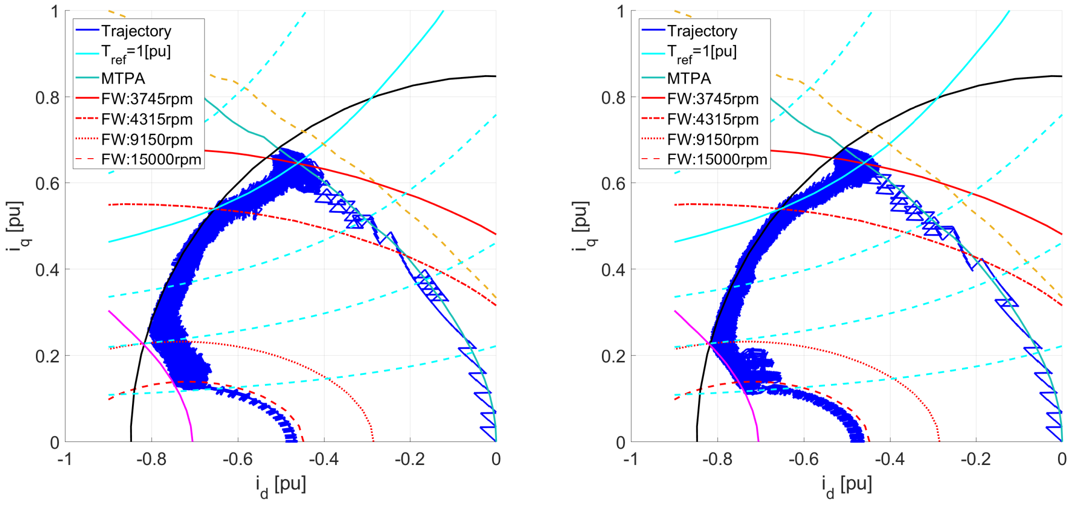

(a) N=2, f_s=48 [kHz] **(b)** N=5, f_s=48 [kHz]

Figure 5.21: Comparison of current states trajectories based on scenario 1

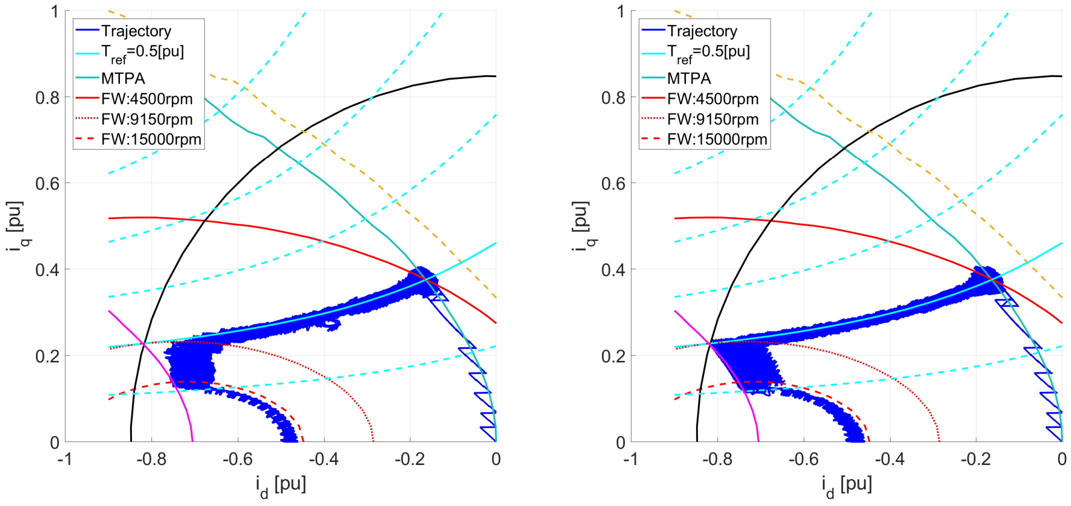

(a) N=2, f_s=48 [kHz] **(b)** N=5, f_s=48 [kHz]

Figure 5.22: Comparison of current states trajectories based on scenario 2

After the higher prediction horizon N=5 is applied to the FCS-MPC, the tracking performances around the MTPV region have been largely improved. The current states can reach the intersection point between the current limit circle and MTPV trajectory and evolving along the MTPV trajectory tightly until the rotational speed reaches 15000 [rpm]. It can be inferred that the tracking bias along the MTPV trajectory at very high speed is due to the inaccurate optimal decision of the FCS-MPC. Since the MTPV cost function is defined as a part of the limitation but not a part of the attraction region, for a short prediction horizon N, the MTPV limitation cost function may not make effect, the point on the left side of the MTPV may be selected as the optimal point. As a result of this, a longer prediction horizon N helps to improve the optimization accuracy.

5.3.2.2 Time plot comparison

The comparisons of the simulation results based on two different prediction horizons are shown in Figure 5.23.

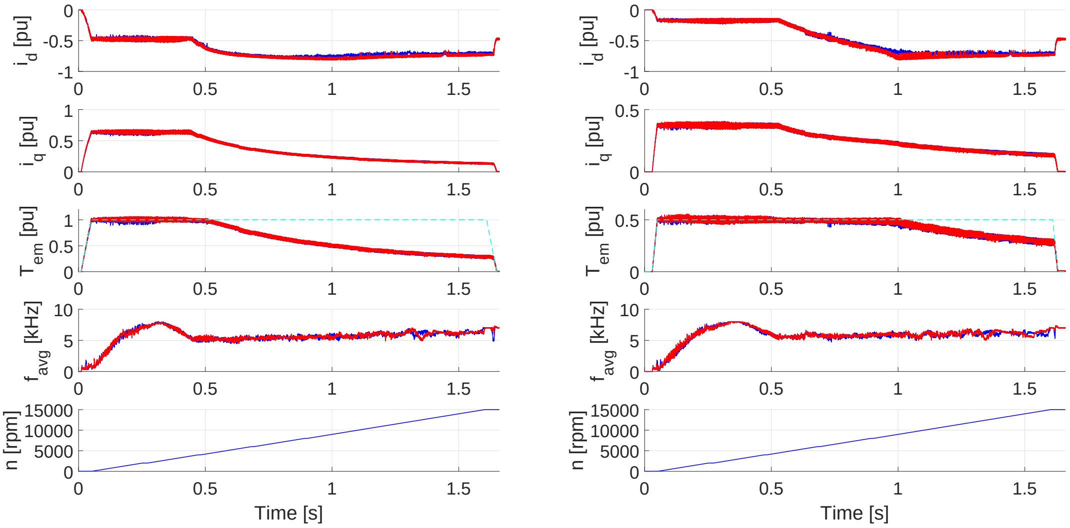

(a) Scenario 1

(b) Scenario 2

Figure 5.23: Comparison of time plots for two scenarios (blue:N=2, red:N=5)

Different from the time plot comparisons based on different switching frequencies, no intuitive difference can be observed for different prediction horizons.

5.3.2.3 Ripple comparison

Figure 5.24 illustrates the steady-state currents and torque time plots which are intercepted from Figure 5.23. Each 0.01 [s] time interval in Figure 5.14 (0-0.01 [s], 0.01-0.02 [s], 0.02-0.03 [s], etc.) represents the steady-state time plots at the speed level of 0 [rpm], 2000 [rpm], 4000 [rpm] and so on.

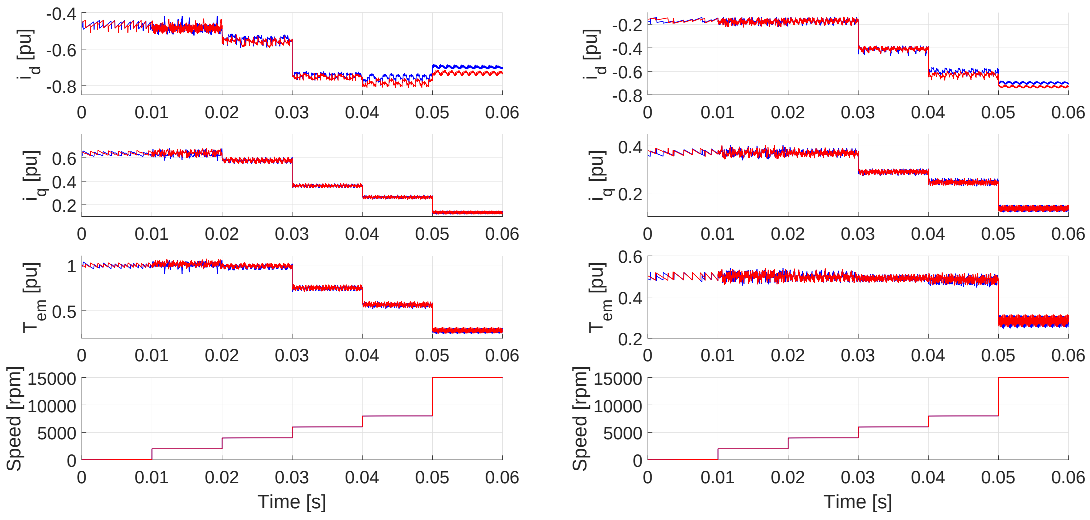

(a) Scenario 1 **(b)** Scenario 2

Figure 5.24: Steady state time plots (blue:N=2, red:N=5)

In general, the steady-state currents and torque based on longer prediction horizon N=5 have similar peak to peak ripple when compared to the default N=2 case.Two bar plots of the peak to peak ripple at different speed levels are presented in Figure 5.25.

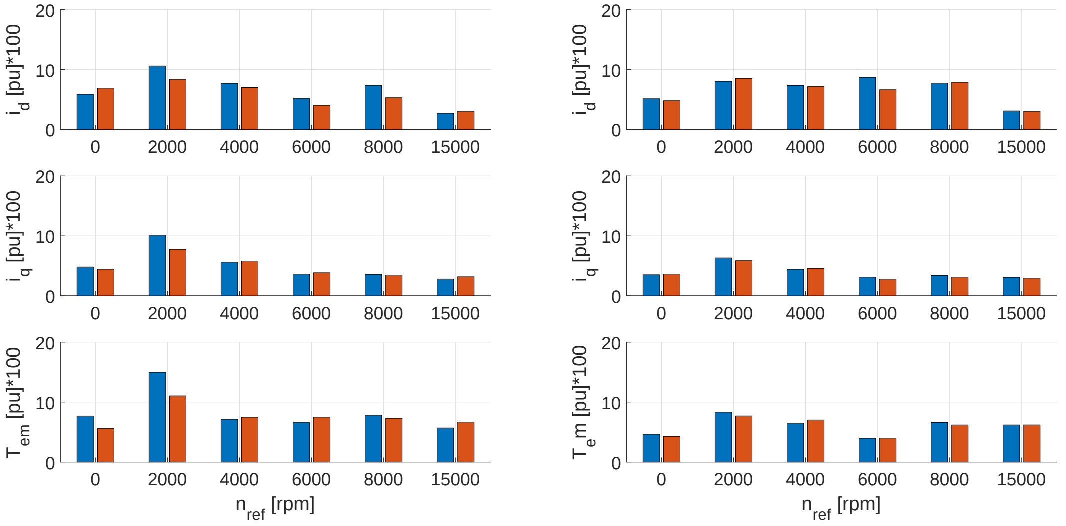

(a) Scenario 1 **(b)** Scenario 2

Figure 5.25: Comparison of ripples for two scenarios (blue:N=2, red:N=5)

According to the results presented above, it can be concluded that increasing the prediction horizon above N=2 gives no significant improvements for the switching losses and currents and torque ripple.

6

Conclusion and Future Work

6.1 Conclusion

In this thesis, a PMSM model consisting of current dependent flux linkages $\psi_d(i_d, i_q)$ and $\psi_q(i_d, i_q)$ is derived. Taking the cross-coupling and flux saturation factors into consideration, the flux linkages ψ_d, ψ_q of the PMSM vary non-linearly with respect to both i_d and i_q. Certain characteristic trajectory functions of the PMSM control strategies such as MTPA, FW and MTPV are reformulated according to the derived PMSM model.

A Finite Control Set Model Predictive Control (FCS-MPC) for the given electric drive system has been developed to realize the automatic switching of the PMSM control strategies such as MTPA and FW. A two-level VSI which only changes its switching states once during one sampling interval is utilized to generate the desired voltage vector for the PMSM. In order to reduce the switching losses, at most one of the three inverter phase legs is allowed to change its switching state between each two sampling instances. Therefore, only 4 of the 8 total switching states can be selected at the next time step. These 4 possible switching states combined with the discretized PMSM model are applied to the FCS-MPC to predict the future system states until the prediction horizon is reached. The optimal switching state for the next time step is evaluated by the cost function.

The cost function is composed of three parts: torque tracking, attraction region and limitation. The torque tracking part enables the PMSM model to generate the electromagnetic torque as the torque reference signal required. The attraction region part decides which control strategies between MTPA and FW is needed based on the torque and speed level, and attracts the current states to evolve on the desired operation trajectory. The limitation part aims to avoid the current states reaching undesired operation regions.

The performance of the FCS-MPC in various operation regions is evaluated from different perspectives. A given benchmark PI controller with a two-level VSI using SVPWM is used to compare the differences between these two control schemes. For the step response comparison, the FCS-MPC has a better performance with no overshoot and lower rise time when it is compared to the PI. The simulation results based on the two scenarios as described in Chapter 4 proves that the current and torque ripple under FCS-MPC are always more than twice as much as the rippes under PI, the ripple differences decrease as the rotational speed goes up. The current states under PI have a better tracking performance along the MTPA trajectory with relatively negligible ripple. The switching losses under FCS-MPC are always lower than that of the PI control scheme.

From the comparisons of the FCS-MPC based on different configurations, for the tracking performance at very high speed, it can be concluded that a higher sampling frequency helps to solve the tracking bias problem along the very high speed FW trajectory (15000 [rpm] in the two scenarios) and a higher prediction horizon enables to improve the tracking performance along the MTPV trajectory. The currents and torque ripple can be reduced if a higher sampling frequency is applied. Also, a higher sampling frequency leads to a lower switching states change percentage during the FW operation region with $T_{em} < T_{ref}$. However, these influences are not obvious for longer prediction horizons.

6.2 Future work

This thesis focuses on the realization of the FCS-MPC for a parameter varying PMSM model. In the future work, several aspects can be included as

- Operation performances of the FCS-MPC when taking temperature variation, measurement noise and error estimation of the PMSM parameters into account.
- Additional cost functions to improve the FCS-MPC performances from different perspectives (e.g. the current and torque quality).
- Differences if a higher level voltage source inverter with matched switching states pre-selection scheme is utilized.
- Realize the auto-tuning of the cost weights when the PMSM operates at different torque and speed levels.

7

Discussion

7.1 Sustainability aspects

In recent years, sustainable development has become a hot topic in media and academic circles. As a result of this, more and more people are concerned and worried about the sustainability problems. In this thesis, a discussion of the PMSM sustainability is made based on the three pillars: ecological aspect, economic aspect and social aspect.

1. Ecological aspect
The traditional combustion vehicles will inevitably emit harmful gases and greenhouse gases. If more electric vehicles are put into use, it is possible to reduce the air pollution and mitigate the impact on the atmosphere. Fundamentally, decarbonization is the long-term issue for the electric systems especially for the fossil fuel power station.

2. Economic aspect
This thesis focuses on the realization of the FCS-MPC control scheme on a nonlinear PMSM model, where the performance of switching losses has been reduced when compared to the benchmark system using PI control scheme. In addition, the rare-earth magnets can produce stronger magnetic fields than the traditional ferrite magnets, and their prices are getting more competitive. A higher efficiency and power density of the electric drives can save cost of an electric vehicles, which attracts more consumers to purchase an electric car instead of a fuel car.

Since both research on and applications of combustion vehicles are relatively mature compared with that of electric vehicles, heavy investment is needed for the research and development of electric drives which could decrease the cost of related products.

3. Social aspect
Nowadays, the safety issues of electric vehicles have aroused people's attention. According to the reports, the electric vehicle accidents are most relevant to the batteries. In order to ensure the safety and reliability of the batteries, it is necessary to realise a deep and comprehensive research of the batteries.

Even though the continuous development of the electric vehicles will create more job opportunities in this industry, it will also bring changes to the automotive market. Social problems may arise such as unemployment and career transition for the traditional vehicle industry.

7.2 Code of ethics

A code of ethics needs to be strictly followed when working on the thesis. Since our thesis is conducted at the company Volvo Group and the electric drive system is supported by our supervisors, we should undertake the confidentiality and ensure no undesired flow of confidential information. Besides, it is important to be honest when deriving results from the acquired data, the thesis is accountable for the Volvo Group, Chalmers University of Technology and ourselves. Lastly, to show our respect, the acknowledgement should include all the people who have offered help to us.

Bibliography

[1] Transport emissions, https://ec.europa.eu/clima/policies/transport.

[2] The future of mobility is electric, https://www.bmvi.de/SharedDocs/EN/Dossier/Electric-Mobility-Sector/electric-mobility-sector.html.

[3] Adolfo Dannier (April 26th 2019). Overview of Main Electric Subsystems of Zero-Emission Vehicles, Propulsion Systems, Alessandro Serpi and Mario Porru, IntechOpen, DOI: 10.5772/intechopen.82876.

[4] F. Wang, X. Mei, J. Rodriguez and R. Kennel, "Model predictive control for electrical drive systems-an overview," in CES Transactions on Electrical Machines and Systems, vol. 1, no. 3, pp. 219-230, September 2017.

[5] C. Schnurr, S. Hohmann and J. Kolb, "Non-linear MPC for winding loss optimised torque control of anisotropic PMSM," in The Journal of Engineering, vol. 2019, no. 17, pp. 4252-4256, 6 2019.

[6] Z. Chen, J. Qiu and M. Jin, "Adaptive finite-control-set model predictive current control for IPMSM drives with inductance variation," in IET Electric Power Applications, vol. 11, no. 5, pp. 874-884, 5 2017.

[7] M. S. Rana, H. R. Pota and I. R. Petersen, "Cross-coupling effect compensation of an AFM piezoelectric tube scanner for improved nanopositioning," 2014 American Control Conference, Portland, OR, 2014, pp. 2456-2461.

[8] M. Preindl and S. Bolognani, "Model Predictive Direct Torque Control With Finite Control Set for PMSM Drive Systems, Part 1: Maximum Torque Per Ampere Operation," in IEEE Transactions on Industrial Informatics, vol. 9, no. 4, pp. 1912-1921, Nov. 2013.

[9] M. Preindl and S. Bolognani, "Model Predictive Direct Torque Control With Finite Control Set for PMSM Drive Systems, Part 2: Field Weakening Operation," in IEEE Transactions on Industrial Informatics, vol. 9, no. 2, pp. 648-657, May 2013.

[10] B. Stumberger, G. Stumberger, D. Dolinar, A. Hamler and M. Trlep, "Evaluation of saturation and cross-magnetization effects in interior permanent-magnet synchronous motor," in IEEE Transactions on Industry Applications, vol. 39, no. 5, pp. 1264-1271, Sept.-Oct. 2003.

[11] P. Lin, W. Lee, S. Chen, J. Hwang and Y. Lai, "Infinite speed drives control with MTPA and MTPV for interior permanent magnet synchronous motor," IECON 2014 - 40th Annual Conference of the IEEE Industrial Electronics Society, Dallas, TX, 2014, pp. 668-674.

[12] A. Mora, Á. Orellana, J. Juliet and R. Cárdenas, "Model Predictive Torque Control for Torque Ripple Compensation in Variable-Speed PMSMs," in IEEE Transactions on Industrial Electronics, vol. 63, no. 7, pp. 4584-4592, July 2016.

[13] Hoffmann, Laurence D.; Bradley, Gerald L. (2004). Calculus for Business, Economics, and the Social and Life Sciences (8th ed.). pp. 575588. ISBN 0-07-242432-X.

[14] B. Zhang, W. Lan, S. Shen and H. Tu, "Jordan Normal Form Based Characteristic Modeling for Multivariable Linear Time Invariant Systems," 2011 Fourth International Conference on Intelligent Computation Technology and Automation, Shenzhen, Guangdong, 2011, pp. 673-675.

[15] I. Takahashi and T. Noguchi, A new quick response and high efficiency control strategy of an IM, in Proc. IEEE IAS, 1985, pp. 16651675.

[16] J. H. Lee, Model predictive control: Review of the three decades of development, Int. J. Contr. Autom. Syst., vol. 9, no. 3, pp. 415424, 2011.

[17] P. Cortes, M. P. Kazmierkowski, R. M. Kennel, D. E. Quevedo and J. Rodriguez, "Predictive Control in Power Electronics and Drives," in IEEE Transactions on Industrial Electronics, vol. 55, no. 12, pp. 4312-4324, Dec. 2008.

[18] F. Sevilmi and H. Karaca, "Simulation and analysis of SVPWM based VSI for wind energy systems," Proceedings of the 2014 6th International Conference on Electronics, Computers and Artificial Intelligence (ECAI), Bucharest, 2014, pp. 73-78.

[19] W. S. Levine, The Control Handbook. Boca Raton, FL: CRC Press, 1996.

[20] Y. Zhang and H. Yang, "Model Predictive Torque Control of Induction Motor Drives With Optimal Duty Cycle Control," in IEEE Transactions on Power Electronics, vol. 29, no. 12, pp. 6593-6603, Dec. 2014.

[21] Y. Zhang and H. Yang, "Model-Predictive Flux Control of Induction Motor Drives With Switching Instant Optimization," in IEEE Transactions on Energy Conversion, vol. 30, no. 3, pp. 1113-1122, Sept. 2015.